Portland State University

PDXScholar

Civil and Environmental Engineering Faculty Publications and Presentations

Civil and Environmental Engineering

1-1-2003

A Multi-Class Suspended Particulate Matter Calibration for Bottom Boundary Layers

Philip M. Orton
Portland State University

David A. Jay
Portland State University

D. J. Wilson
Oregon Health & Science University

Follow this and additional works at: https://pdxscholar.library.pdx.edu/cengin_fac

Part of the Civil and Environmental Engineering Commons

Let us know how access to this document benefits you.

Citation Details

Orton, Philip M.; Jay, David A.; and Wilson, D. J., "A Multi-Class Suspended Particulate Matter Calibration for Bottom Boundary Layers" (2003). *Civil and Environmental Engineering Faculty Publications and Presentations*. 32.
https://pdxscholar.library.pdx.edu/cengin_fac/32

This Post-Print is brought to you for free and open access. It has been accepted for inclusion in Civil and Environmental Engineering Faculty Publications and Presentations by an authorized administrator of PDXScholar. Please contact us if we can make this document more accessible: pdxscholar@pdx.edu.

Submitted to *Marine Geology*, April 3, 2003

A multi-class suspended particulate matter calibration for bottom boundary layers

P.M. Orton[a], D.A. Jay[a*], and D.J. Wilson[a,b]

[a] Department of Environmental and Biomolecular Systems, OGI
School of Science and Engineering, Oregon Health & Science
University, 20000 NW Walker Rd., Beaverton, OR 97006, USA

[b] Now at: Imagenex Technology Corp., 209-1875 Broadway St., Port
Coquitlam, British Columbia, Canada, V3C 4Z1

* Corresponding author. Fax: (503) 748-1273; email:
djay@ese.ogi.edu

Abstract

We present a multi-class suspended particulate matter (SPM) calibration for use with *in situ* water sample SPM concentration data and backscatter (or transmission) from one or more acoustic and optical sensors. The output of this calibration is high-resolution SPM concentration data in several discrete settling velocity (*Ws*) classes. Separately for each sensor, the calibration involves three steps: (1) a calibration of backscatter to total SPM concentration; (2) a decomposition of resulting concentration data into several *Ws*-classes, utilizing a dynamical vertical SPM profile model; and (3) a sensor bias calibration where water sample concentration data are used to correct for the sediment size-dependence of sensor response. Multiple sensors can be incorporated to improve the results, as step 3 can objectively choose the best sensor for monitoring each *Ws*-class. The calibration is generally applicable in wave-current boundary layers, though this paper is focused on currents only. We demonstrate the method using data from greater-ebb SPM export events in the Fraser River estuary, when salt has washed out beyond the river entrance, surface currents are strong (3+ m s^{-1}) and turbulent mixing is intense. The resulting concentration estimates show good agreement with *in situ* particle-size observations near the bed, but discrepancies increasing with height above the bed, likely due to violation of model assumptions in the outer part of the water column. An uncertainty analysis indicates that the standard deviation in concentration estimates is 32-48%, primarily due to poor near-bed acoustic data coverage and uncertainty in water sample concentration data. We conclude by discussing planned improvements for strongly advective and aggregate-dominated systems.

Keywords: Suspended materials; Particle settling velocity; Concentration; Backscatter; Calibration; Inverse methods

1. Introduction

Suspended particulate matter (SPM) transport and deposition in aquatic systems is strongly constrained by the settling velocity (*Ws*) of the sediments of interest (Dyer, 1986; Kineke and Sternberg, 1989). Observations show that SPM is typically heterogeneous, with a broad and highly variable spectrum of *Ws* values, and correspondingly diverse transport patterns. Different classes of SPM also have specific geological, chemical, and ecological influences during and after transport (Dyer, 1986; Sherwood *et al.*, 2002). In workshops focused on the development and evaluation of a community coastal SPM transport model, researchers have stressed the need for observations of SPM concentration (*C*) across a wide range of sediment classes (Sherwood *et al.*, 2002).

Unfortunately, observational techniques are often insufficient for model verification or monitoring needs. It is possible to directly measure *in situ C* and *Ws*, yet these measurements do not have the spatial and temporal resolution necessary for most applications. The most common high-resolution techniques rely on “bulk” sediment calibrations, where total *C* is monitored, ignoring *Ws* (Thevenot and Krauss, 1993; Bunt *et al*., 1999). A drawback of bulk SPM concentration calibrations is that the response of an acoustic or optical SPM sensor is a strong function not only of C, but also particle characteristics (diameter, shape and density). Most sensors respond strongly only to a narrow range of SPM sizes, and a bulk calibration often incurs biases if particle characteristics are variable (Bunt *et al*., 1999; Thorne and Hanes, 2002).

We have developed a model-dependent multi-class SPM calibration to avoid these limitations. The calibration provides high-resolution C data in several discrete “Ws-classes”. Not only can the approach be applied in future SPM transport studies, but also to extensive archives of data from prior studies; it only requires *in situ* water sample C data and backscatter (or transmission) profiles from one or more acoustic or optical sensors. The calibration corrects for the dependence of sensor response on particle diameter. Data from multiple sensors can be incorporated to widen the detected particle size range and improve the accuracy of the resulting C estimates. Simulations suggest that the method can resolve eight or more Ws-classes if backscatter data have high vertical resolution and low noise levels. Near-synoptic spatial coverage is possible, but noise levels are typically higher for mobile sampling strategies, reducing the number of Ws-classes that can be resolved.

In this paper, we: (a) describe the calibration methodology; (b) apply the method to study Fraser River sediment export; (c) quantify uncertainty and determine where calibration assumptions are violated; and (d) discuss optimization, benefits and drawbacks for this new calibration approach. We also explain that our calibrated observations are interchangeable with direct measurements of Ws and C, and can help provide high-resolution, spatially distributed multi-class SPM data useful for evaluating three-dimensional models.

2. Background

Several approaches have been developed for *in situ* monitoring of multi-class SPM. There are four main approaches for partitioning observed *C* data into different sediment classes (Dyer *et al*., 1996; Agrawal and Pottsmith, 2000; Thorne and Hanes, 2002): (a) settling chambers, (b) underwater video, (c) multi-frequency backscatter techniques, and (d) laser-diffraction methods. While these approaches have improved our ability to monitor sediment transport, all have important limitations. Settling chambers and underwater video are difficult to deploy in environments with high levels of shear or turbulence, have extremely limited spatial and temporal resolution, and give concentration-dependent results. These systems also alter the hydrodynamic environment of trapped particles, changing settling rates of aggregated fine sediments (Milligan, 1995). Different settling tube techniques commonly give *Ws* estimates that vary by an order of magnitude (Dyer *et al.*, 1996). Video techniques are unable to distinguish finer particles, and thus estimation of *C* data in slow-settling *Ws*-classes is difficult (Fennessy and Dyer, 1996). At the very least, it would be useful to verify the many published settling tube and video 'observations' of aggregate *Ws* with data from a non-intrusive method such as the one presented in this paper.

Laser-diffraction and multi-frequency acoustic methods are useful because they can provide *in situ* high frequency, relatively non-intrusive measurements of *C* in several size-classes. However, these approaches do not provide a complete solution for suspensions that include aggregates, because they rely on inversion algorithms that incorporate shape and/or density assumptions. The particle size range of these methods is often limited, and multi-modal size distributions are usually problematic. Furthermore, these methods provide size-class partitioned C data; direct measurements of Ws-class partitioned C are only available with use of a paired settling chamber (Agrawal and Pottsmith, 2000; Thorne and Hanes, 2002). Finally, for dynamical studies it is better to avoid using particle diameter (D) as an intermediary for Ws; uncertainty in particle size is amplified in the conversion to Ws because $Ws \propto D^2$ for fine sands and finer sediments (Gibbs *et al*., 1971).

3. Calibration Methodology

Our multi-class SPM calibration, summarized in **Figure 1**, involves three steps: (1) a total SPM calibration that provides a reasonable initial estimate of C; (2) a model-dependent decomposition of these C data into several Ws-classes; and (3) a sensor bias calibration where water sample C data are used to correct for the sediment size-dependence of sensor response. Multiple sensors can be incorporated to improve the results, as step (3) can objectively choose the best sensor for monitoring each Ws-class.

3.1. Step 1: Total SPM calibration

A total (bulk) SPM calibration provides reasonable initial estimates of C for our multi-class calibration technique. A total SPM calibration is performed separately for each acoustic and optical sensor, through comparison with *in situ* water sample SPM concentration data ($C_{watersample}$). Common sensors include those that measure optical backscatter (OBS) or transmission (summarized in Bunt *et al*., 1999), acoustic backscatter pressure (summarized in Thorne and Hanes, 2002), or acoustic backscatter (ABS) from Doppler current profilers (Thevenot and Krauss, 1993; Deines, 1999). As mentioned above, this initial bulk calibration has two major drawbacks: it determines only total *C*, and it can incur biases if the SPM field is heterogeneous. Steps 2 and 3 of our multi-class SPM calibration eliminate these limitations.

3.2. Step 2: Model-dependent decomposition

In the model-dependent decomposition, a dynamical vertical SPM model is used to partition *C* data from Step 1 into several *Ws*-classes. This model should be practical and fast, with a computation time of no more than one day for thousands of profiles. The only free variables must be *Ws*, which determines the profile slope, and a reference concentration (C_a) that scales the profile; other unknowns must be estimated from theory and observations. In this paper, we utilize a model for current boundary layers only (Hill et al, 1988), but many wave-current boundary layer models also have these characteristics (Davies *et al.*, 2002). A set of *Ws* values is chosen to represent the *Ws*-classes that might be in suspension, then the model is used to create a basis function (profile shape) for each *Ws*-class. The scaling (C_a) for each *Ws*-class is set with a least-squares regression so that their sum most closely approximates the total *C* from Step 1 (**Figure 2**).

A SPM profile model for steady or quasi-steady current boundary layers can be derived from simplifications of the mass conservation equation for SPM in a transporting fluid.

Neglecting horizontal turbulent mixing, the SPM conservation equation for a single *Ws*-class may be written:

$$\frac{\partial C_j}{\partial t}+u\frac{\partial C_j}{\partial x}+v\frac{\partial C_j}{\partial y}+w\frac{\partial C_j}{\partial z}=Ws_j\frac{\partial C_j}{\partial z}+\frac{\partial}{\partial z}\left(K_{s,j}\frac{\partial C_j}{\partial z}\right)+S_j \qquad (1)$$

This involves C_j, the mass SPM concentration for *Ws*-class *j*; time, *t*; horizontal velocities, *u* and v, in horizontal dimensions, *x and y*; vertical velocity, *w*; height above the bed, *z*; and the mass diffusivity for sediment, $K_{s,j}$; and a source-sink term S_j that accounts for aggregation and disaggregation. If vertical diffusion and settling terms dominate over advection, time evolution, and non-conservative behavior, and *C* at height above the bed $z = z_a$ is specified as a boundary condition (the reference concentration, $C_{a,j}$), one obtains:

$$C_j(z)=C_{a,j}\exp\left(Ws_j\int_{z_a}^{z}\frac{dz}{K_{s,j}(z)}\right) \qquad (2)$$

This is a generalization of the Rouse equation, an analytical solution obtained through use of a parabolic $K_{s,j}$ profile. Several studies have verified the applicability of eq. (2) to a wide range of conditions in laboratory and field conditions (summarized in Hill *et al.*, 1988). Inverse analysis has previously been applied to the function shown in eq. (2), as knowledge of $C_j(z)$, the 'dependent' variable, is often available when one of the 'independent' variables $C_{a,j}$, Ws_j, or $K_{s,j}$ is not (*e.g.* Hill *et al.*, 1988; Orton and Kineke, 2001; Rose and Thorne, 2001).

The total *C* for a multi-class particle suspension is the sum of eq. (2) as applied separately to each discrete settling velocity class, *j* = (1,*n*). Acknowledging that this is a common inverse analysis problem (Menke, 1989), we introduce the inversion kernel, G_{ij} the discretized numerical solution to the exponential term in eq. (2) for each *Ws*-class *j*, at heights z_i [i=(1,m)]:

$$C_i = \sum_{j=1}^{n} C'_{a,j} G_{ij} = \sum_{j=1}^{n} C'_{ij} \tag{3}$$

Here, C_i is the concentration profile measured by a given sensor, and $C'_{a,j}$ is the set of unknown reference concentration data. A set of reasonable Ws_j values and estimates of $K_{s,ij}$ are used to calculate matrix G_{ij}, then combined with observations of C_i to solve for $C'_{a,j}$, using a multivariate non-negative linear least-squares algorithm. Knowledge of $C'_{a,j}$ and G_{ij} then provides the 'best-fit' concentration profiles for each *Ws*-class, C'_{ij}. **Figure 2** shows decomposition results for acoustic and optical *C* estimates from the same water column. This approach has been applied and verified previously with data from the Columbia River estuary, as described in Fain *et al*. (2001). It is desirable to favor data points in the near-bed region, where the assumptions used in deriving eq. (2) are most likely to be satisfied. This can be accomplished using a weighted least-squares algorithm.

3.3. Step 3: Sensor bias calibration

Different sensors typically respond best to different particle sizes, and generally disagree on the distribution of *C* over *Ws*-classes (C'_{ij}). This is because backscatter or transmission is a function not only of *C*, but also the signal wavelength (or frequency) of the sensor and the SPM particle size spectrum. This is most obvious when contrasting the response of an optical and an acoustic sensor, because there is typically a three orders-of-magnitude difference in signal wavelength. This is also true for optical or acoustic sensors with differing wavelengths, though the differences may be more subtle (Hatcher *et al.*, 2000; Thorne and Hanes, 2002).

Bulk SPM calibrations mask these sensor response differences, as shown by the similarity of the optical and acoustic total concentration (C_{OBS} and C_{ABS}) profiles in **Figure 2**. Nonetheless, the SPM particles that are controlling sensor response in each case are quite different. Using scattering theory, one can estimate the response of a sensor to a given particle size spectrum (**Figure 3**). Optical sensors are more sensitive to fine sediments, while acoustic sensors are more sensitive to sands. Based on the geometric optics theory, OBS for particles larger than ~1 μm is inversely proportional to the square root of particle diameter, $\propto D^{-0.5}$ (Lynch and Agrawal, 1991). The ABS response of a 1200 kHz acoustic sensor has two theoretical regimes; the particles under ~100 μm are in the Rayleigh scattering regime, where the dependence upon diameter is strong, $\propto D^3$; for larger particles, the dependence upon D weakens, with a transition to geometric scattering (Clay and Medwin, 1977).

Lynch and Agrawal (1991) utilize scattering theory to correct for the size-dependent response bias of each sensor. This approach requires particle shape and density assumptions that are uncertain for suspensions that include aggregated particles. For the case of geometric scattering, it also requires the assumption that particles are not shading one another, unrealistic with high SPM concentrations. In Step 3 of our calibration, we instead use $C_{watersample}$ data to calibrate and correct for sensor bias. With OBS or ABS, it is reasonable to assume that different SPM size fractions produce partial sensor responses as though each fraction were the only one present (Green *et al.*, 2000; Hatcher *et al.*, 2000). As a result, one can assign separate linear calibration slopes (g_j) for each *Ws*-class, correcting for the size-bias of the sensor. As was the case with eq. (3), a multivariate linear regression may be used to obtain the unknown parameters, g_j:

$$\mathbf{C}_{watersample,k} = \sum_{j=1}^{n} g_j\, C'_{jk} \qquad (4)$$

Here, $C_{watersample,k}$ [k=(1,p)] represents a set of p *in situ* C estimates from water samples, and C'_{jk} is the set of matching data points after eq. (3) has been solved for all profiles. Much like the procedure after a bulk SPM calibration, these calibration slopes are then applied to the entire data set:

$$C''_{ij} = g_j\, C'_{ij} \qquad (5)$$

Thus, one obtains the final multi-class SPM concentration data for each profile, C''_{ij}, corrected for the dependence of sensor response on particle size.

3.4. Incorporating multiple sensors

Optimally, one should monitor a given type of SPM with the sensor that is best suited for detecting it. With q sensors of differing signal frequencies, an iterative approach may be used to choose which sensor best responds to C variations in each Ws-class. This involves solving the first equality in eq. (4) several times with q different sensor choices, applied in all possible combinations to the n Ws-classes. Thus, there are q^n different sensor combinations to test. The optimal set of assignments for sensor and Ws-class is the one that minimizes rms differences between C_k and C''_{jk}, though additional subjective considerations may apply (*e.g.* the resolution of the output data set).

4. Application to the Fraser River Estuary

We observed SPM transport processes in the Fraser River estuary from the vessel *R/V Barnes*, during the 1999 and 2000 spring freshets. Cruise dates were July 5-26, 1999, and June 30 - July 4, 2000. Riverflow during the 1999 sampling period was well above normal, at 9000 m^3s^{-1}, while in 2000 it was 7000 m^3s^{-1}, a typical spring freshet level (Water Survey of Canada, unpublished data). The 1999 data are not the focus of this paper, but included additional measurements (discussed below) that help to put our 2000 observations in context. The Fraser is a river-dominated, strongly-channelized system. Tides are mixed semidiurnal, and the tidal range at the entrance varies from 2 to 5 m. Median bed sediment particle size is typically 250-320 μm, and bedforms in the main channel have heights of O(1 m) and wavelengths of O(20 m). Kostaschuk and Luternauer (1989) and Macdonald and Geyer (2002) give a more complete description of the geography and dynamics of the Fraser estuary.

The 2000 data set includes ~150 transects and a 24-hour anchor station in the lower 10 km of the estuary. **Figure 4** shows two transects at the mouth of the Fraser that will be discussed later in this paper. The instrumentation included (a) a broadband Acoustic Doppler Current Profiler (RD Instruments; 1200 kHz) mounted on the side of the vessel; (b) a winch-deployed *CTD-OBS frame*, carrying an Optical Backscatter Sensor (D&A Instruments), and a Conductivity-Temperature-Depth (CTD) sensor (Ocean Sensors, Model OS200); (c) a separate winch-deployed *calibration frame* with another OS200 CTD, an Optical Backscatter Sensor, a 1.5 L Niskin water sample bottle (General Oceanics, Model 1010), and a Laser *In Situ* Scattering and Transmissometry (LISST) instrument measuring particle sizes from 5-500 μm (Sequoia Scientific, Model 100A); (d) and an analog Echo Sounder (Ross Laboratories, Model 803, 200 kHz).

The ADCP provided continuous remote current velocity and ABS profiles with 0.25 m vertical resolution. Due to the 20^o beam-angles, data in the lower 8% of the water column near the bed were lost due to bed-reflection effects; profiles typically begin at $z \cong 1.0$ m in a 10 m depth water column. ABS data for each of the four acoustic beams were processed separately, according to methods described in Deines (1999). In regions with large bedforms, ADCP data were smoothed (running average) over a distance of 90 m, three times the median bedform wavelength. The *CTD-OBS frame* allowed rapid water column profiling of temperature, salinity and OBS. Sampling strategies included stationary water column profiling and a transect to-yo mode where the moving vessel towed the frame while it was profiled through the water column. The *calibration frame* collected water samples for calibration of the OBS and ABS sensors, as well as *in situ* particle size data. It was used less frequently to collect vertical profiles of the *in situ* sediment particle size spectrum (LISST-100A, 5-500 μm size range), optical transmission, OBS, temperature, and salinity. A trigger fired upon contact with the bed, causing a water sample to be taken at $z \cong 0.55$ m. These samples, and surface samples collected by bucket, were used to gravimetrically calibrate OBS and ABS to total SPM concentration (**Figure 5**) and to constrain the sensor bias correction, as outlined in **Figure 1**.

In 1999, similar measurements were made aboard the *Barnes*. Scientists aboard a second vessel, the *R/V Sproul*, also measured total *C* and zooplankton counts from pumped water samples, particle settling velocity (determined with a modified Owen settling tube; Reed and Donovan, 1995), and disaggregated particle sizes (from a Coulter Counter). Due to low numbers of zooplankton (C. Simenstad, unpublished data) and the low acoustic reflectivity of estuarine species types (Stanton *et al*., 1998), zooplankton do not provide comparable backscatter to suspended sediments. This condition was assumed to apply in 2000, as well.

4.1. Fraser observations

For this paper, we have applied our multi-class SPM calibration only to observations from greater-ebb SPM export events from June 30 to July 4, 2000. During greater-ebb spring tides, the Fraser River was a zero length estuary for about four hours, in that salt was completely washed out of the estuary, beyond the river entrance. These are dynamically simple periods, because salinity stratification is absent, and the near-bed SPM distribution is predominantly determined by vertical diffusion and settling. They are also of significant geological interest, because most sand export to the Fraser delta occurs under these conditions (Kostaschuk and Luternauer, 1989). Thus, these greater-ebb SPM export events are useful as a simple test for our new calibration technique. Tides during the 2000 cruise were near spring phase, with a spring-tide on July 2; tidal ranges were 4.0 - 4.4 m. Winds were generally under 5 m s^{-1}, and wave heights in the estuary were <0.5 m. During periods with high *C*, the water column was weakly stratified by high levels of suspended sediment. Data from a representative transect (T193, **Figure 4**) are shown in

Figure 6. These conditions were typical of the greater-ebb SPM export events, with strong surface currents (3+ m s^{-1}) and intense turbulent mixing.

LISST-100 *in situ* particle size distributions for four heights above the bed on the landward end of T193 are shown in **Figure 7**. The LISST volume concentration output was separated into two realms for the conversion to relative mass concentration. For particles from 5-350 μm, a “negligible aggregation assumption” was used; particles without aggregation should have a density near that of quartz, 2650 kg m^{-3}. A useful index of aggregation is the ratio of median disaggregated particle diameter to the diameter calculated for the median Owen tube *Ws* (Reed and Donovan, 1995). For the 1999 freshwater SPM samples, this ratio was typically no higher than unity (D. Reed, unpubl. data), indicating that the assumption of minimal aggregation was reasonable.

For particles observed with the LISST in the size range from 350-500 μm, a laboratory disaggregated particle size analysis was used to determine whether these particles were aggregates or sand particles. For periods with strong turbulence, sand particles dominated, and the negligible aggregate assumption was used. For cases where no primary particles from 350-500 μm were present, the particles were assumed to be aggregates. Observations show that a reasonable effective density estimate for large aggregates is 160 kg m^{-3} (Dyer and Manning, 1999), and this value was used to convert volume to mass. At this density, and using the LISST spectra, these large aggregates were likely to amount to no more than 5% of total mass concentration.

4.2. Fraser parameterizations

We performed the multi-class SPM calibration for a two-sensor combination of OBS and ABS, with three *Ws*-classes. To favor near-bed data, linear weighting of $(h\text{-}z)/h$ was applied for the regression in Step 2, as suggested in **Section 3.2**. Important parameterizations for Step 2 are described below, including *Ws*-classes and a representation of turbulent mixing in a sediment-stratified flow.

4.2.1. *Ws*-class definitions, motivation

The LISST and settling tube observations indicate that the SPM in suspension during greater-ebb SPM export events can be characterized by three *Ws*-classes (Ws_j = 0.01, 10, 37 mm s^{-1}; **Table 1**). A nominal *Ws* of 0.01 mm s^{-1} applies to the slow-settling *Ws*-class (washload). The central *Ws*-class corresponds to disaggregated settling for the main peak in the LISST particle size distribution. The rapid-settling *Ws*-class corresponds to the median bed-sediment particle size of 300 μm (Kostaschuk and Luternauer, 1989). Simple simulations of the SPM decomposition with artificial data show that each *Ws*-class corresponds to a range in *Ws*, and these ranges are shown in **Table 1**. Settling velocities were calculated using Stokes Law and an intermediate diameter settling equation (Gibbs *et al*., 1971), with the assumption that particles were quartz spheres. Sample *C* profiles calculated from eq. (2) for these *Ws*-classes are shown in **Figure 2**.

4.2.2. Vertical diffusion of momentum

We used a linear-exponential neutral eddy diffusivity for momentum (K_0) to estimate the sediment diffusivity ($K_{s,j}$) for the quasi-steady tidal currents experienced in the Fraser:

$$K_0 = kU_* z\, e^{-z/L} \qquad (6)$$

Stratification effects and the conversion to mass diffusion are considered below in **Section 4.2.3**. The formulation in eq. (6) has been extensively tested against data from marine and atmospheric boundary layers (Long, 1981; Beach and Sternberg, 1989). Parameters include the boundary layer length scale $L = h/3$, von Kàrmàn's constant, $k \cong 0.41$, and the shear velocity $U_* = \sqrt{t_0 / r}$, a convenient proxy for the shear stress at the bed t_0. A quadratic drag law may be used to estimate t_0, and thus U_* (Sternberg, 1972):

$$t_0 = r c_{D,b} U_{\mathrm{b}}^2 \qquad (7)$$

Here, b is the drag coefficient reference level, and U_b is the mean velocity at $z = b$. Due to bedforms in the Fraser, the total bedstress (t_0) differs substantially from the skin friction bedstress. Zyserman and Fredsoe (1994) used flume data to demonstrate that while sediment entrainment is controlled by skin friction, the C profile shape is controlled by t_0. Total bedstress can be calculated using eq. (7), as long as the drag coefficient reference height (b) is well above the height of the bedforms. For this reason, we applied eq. (7) with $b = 3$ m.

For hydrodynamically rough flow, the effect of bedforms on the drag coefficient can be estimated as (Dade *et al.*, 2001):

$$c_{D,b}^{-0.5} = (1/k) \ln(b/z_0) \quad \text{where } z_0 \cong k_N / 30 \qquad (8)$$

Above, z_0 is the apparent hydraulic roughness length, and the apparent Nikuradse roughness length (k_N) was modeled as form drag due to bedforms (Grant and Madsen, 1982):

$$k_N = 27.7\, H_{bf}^{2} / L_{bf} \tag{9}$$

Contributions to k_N from grain roughness and moveable bed roughness (suspended sediment) are negligible for the Fraser observations, and thus are not present in eq. (9). Our echo sounder data allowed us to directly measure the median bedform height (H_{bf}) and wavelength (L_{bf}) during transects, and thus calculate $c_{D,300}$. Bedforms were small along T192 (**Figure 4**; $H_{bf} = 0.2$ m; $L_{bf} = 5$ m; $c_{D,300} = 0.0044$). T193 had an abrupt change at $x = 0.5$ km (**Figure 6**), with smaller bedforms seaward ($H_{bf} = 0.2$ m; $L_{bf} = 10$ m; $c_{D,300} = 0.0036$) and larger bedforms landward ($H_{bf} = 1.1$; $L_{bf} = 30$; $c_{D,300} = 0.0083$). These drag coefficients were within the range previously observed for neutrally buoyant flows with sandy bedforms, 0.003 - 0.010 (Sternberg, 1972; Chriss and Caldwell, 1982).

4.2.3. Diffusion of sediment in a stratified flow

Though this paper is focused on freshwater flows, the water column was mildly stratified at times due to vertical gradients in SPM concentration. We used a simple algebraic approach to account for turbulence damping of K_0 (eq. 6) due to stratification:

$$K_m = K_0\,(1 + R\,Ri)^{-s} \tag{10}$$

Empirical evidence suggests that constants of $R = 3$ and $s = 3$ are appropriate (Lehfeldt and Bloss, 1989). The gradient Richardson number Ri, is a measure of vertical stability:

$$Ri = -\frac{g}{r}\left(\frac{\partial r}{\partial z}\right)\left(\frac{\partial u}{\partial z}\right)^{-2} \tag{11}$$

Here, g is the gravitational acceleration and r is the local water density. The effects of stratification are negligible for $Ri < 0.03$, and mixing is strongly suppressed when $Ri \geq 0.3$ (Dyer, 1986). For the data used in this study, stratification was weak; Ri was typically below 0.03, and only above 0.10 in 2% of bins. A typical profile of the neutral eddy diffusivity K_0, as well as the stratification-modified diffusivity K_m, is shown in **Figure 8**.

Researchers often assume that $K_m = K_{s,j}$ when they apply the Rouse equation. More generally, a proportionality constant (b_j) should be used, so that $K_{s,j} = b_j K_m$. Recent studies suggest that b_j varies with particle and flow characteristics, and a consensus treatment is summarized by Rose and Thorne (2001):

$$K_{s,j} = b_j K_m \tag{12}$$

$$b_j = 3.1 \exp(-0.17\, U_*/Ws_j) \quad \text{for } 1 <= U_*/Ws_j <= 9.5 \tag{13}$$

The data supporting this relationship show significant scatter, with a standard deviation in b_j of roughly +/- 25%. Calibration uncertainty from this and other turbulence parameters is analyzed in **Section 5**.

4.3. Fraser calibration results and SPM export

The three calibration steps each provided results and a regression coefficient of determination (r^2) as a measure of performance. The bulk calibrations (Step 1; **Figure 5**) for OBS and ABS had r^2 results of 0.71 and 0.54, respectively. The low ABS r^2 was likely due to the impact of particle size variations; ABS is very sensitive to particle size (**Figure 3**). The low r^2 values of both bulk calibrations illustrate the need to calibrate OBS and ABS in terms of individual *Ws*-classes. Small perturbations and methodological differences in the bulk calibrations were found to have little effect on the final concentration output of the multi-class calibration (C''_j), though a large perturbation or erroneous bulk calibration altered the C''_j results. The r^2 for the model-based decomposition (Step 2; **Figure 2**) rates the quality of fit between the initial total concentration estimates (C_{OBS}, C_{ABS}) and the model-based total concentration estimates ($\Sigma C''_j$). These values are shown in the bottom panel of **Figure 9**, for all OBS and ABS decompositions on T193.

We carried out Step 3 (eq. 4), the sensor bias calibration, using all possible combinations of the two sensors for different *Ws*-classes. Only profiles with low stratification ($Ri < 0.1$) and good model-data correspondence ($r^2 > 0.80$) in Step 2 were used in Step 3, to avoid periods when the assumptions of the decomposition model were violated. As expected from **Figure 3**, ABS was not highly responsive to variations in fine sediments (Ws_1). The OBS, on the other hand, responded to variations in all *Ws*-classes. The optimal sensor combination was a "joint" two-sensor calibration, using optical Step 2 results for Ws_1 and Ws_2, and acoustic results for Ws_3. This sensor combination for Step 3 had an r^2 of 0.82 with 25 data points, and the bias calibration slopes were g_1 = [0.76, 1.17, 1.15] (**Figure 10**). The fact that all three slopes were ~1 (*i.e.* the bias corrections were small) is a positive sign, indicating that these sensors were well-chosen for monitoring these *Ws*-classes. For the OBS *Ws*-classes, note that $g_1 < 1$ and $g_2 > 1$. This is in line with expectations for an optical sensor, because Step 3 must correct for the preferential detection of the smallest particles. We found a similar r^2 for Step 3 using OBS for all three *Ws*-classes, but chose to use acoustic results for Ws_3 because of the high-resolution of the data and the likely improved reliability when coarse material dominates.

Applications of the resulting multi-class concentration data (C''_j) include export flux calculations and transect analyses. Fluxes of total C'' were calculated and compared to fluxes of C_{OBS} and C_{ABS}, for two locations at the mouth of the river (**Figure 11**). For these calculations, velocity was extrapolated logarithmically toward the bed, to $z = 0.25$ m, and the export flux is the flux at the river mouth. We chose the two locations to show the across-channel contrast in export; T192 is a shallow water transect and T193 is on the edge of the thalweg (10 m depth). The primary sediment delivered to the upper delta slope, C''_2, is delivered to sea at a much higher rate along T193 than along T192. Bed sediment, C''_3, is delivered almost exclusively along T193. T193 is shown in detail in **Figure 9**, with concentration data for all three Ws-classes, shear velocity and r^2 for Step 2. The r^2 value for most C_{OBS} and C_{ABS} decompositions on T193 was above 0.90. The spatial distribution of the profiles is shown by the r^2 data points, with resolution in C''_1 and C''_2 (from OBS) being significantly less than that in C''_3 (from ABS).

5. Assumptions and Uncertainty

A model is normally assumed to be correct in any calibration of a proxy variable with a desired variable. With a calibration of OBS with SPM concentration, for instance, it is typically assumed that there is a linear relationship between the two variables, and that variables such as particle size and color have a negligible effect on OBS response. Though our calibration involves a dynamical model, there are general similarities with simpler calibrations. In this section, we explain how: (a) conditions that render the model assumptions inappropriate can be diagnosed; and (b) uncertainty in calibration slopes and final concentration data can be quantified for cases when the model is appropriate. In **Section 6.1**, we discuss how a sampling strategy can be optimized to improve the quality of calibration results.

5.1. Evaluating assumptions

It is important to evaluate whether the model employed in Step 2 is appropriate for the environment being studied. The evaluation of model assumptions can be carried out in two ways. One can directly evaluate the SPM dynamic balance (eq. 1), or flag cases where the model-data fit in Step 2 is poor. In using a vertical SPM distribution model (eq. 2), we have assumed that turbulent diffusion and particle settling dominate the dynamic balance for suspended sediment. We calculated the horizontal average of each dynamic balance term in eq. (1) for each transect (*e.g.* **Figure 12**) to evaluate this assumption. A constant Ws was assumed in these calculations, using the modal settling velocity in the near-bed region (Ws = 7 mm s^{-1}; **Figure 7**). Derivatives were estimated using observations and eddy diffusivity ($K_{s,j}$) calculations (eqs. 6-13). If the terms are all accounted for and accurate, the discrepancy, or sum of all signed terms, should balance out to zero. The discrepancy was typically small but nonzero, because of inaccuracies in the estimated dynamic terms or because S_j (aggregation and disaggregation) could not be accounted for in the analysis. Settling and diffusion dominate in the near-bed region, where other terms are typically smaller by at least a factor of 10. The advection and discrepancy terms may be of comparable magnitude in the middle and outer water column. This justifies the weighting of the least-squares analysis for eq. (3) by the factor

$(h\text{-}z)/h$, as discussed in **Section 3.2**, causing the near-bed data points to be weighted more heavily than those near the surface.

Another means of evaluating the applicability of the dynamical model is the aforementioned coefficient of determination for the regression, r^2. High r^2 values (**Figure 9**, bottom panel) do not prove that the model is appropriate, but they do bolster our case. Another use of the Step 2 r^2 values is to locate profiles where the diffusion-settling balance appears to break down, and objectively omit them from calibration Step 3.

5.2. Quantifying uncertainty

Uncertainty (standard deviation, s) in model parameters and observations leads to uncertainty in the results of the model-dependent decomposition ($C'_{a,j}$) and settling velocity class center-points (Ws_j). The uncertainty in $C'_{a,j}$ maps into uncertainty in the sensor bias calibration slopes (g_j), and uncertainty in the final multi-class concentration data (C''_j). In this section, we summarize previous uncertainty analyses of similar SPM decompositions, explain a Monte Carlo randomization approach to estimating uncertainty, and then discuss uncertainty analysis results.

Previous uncertainty analyses of model-dependent SPM decompositions have shown that such decompositions have limited resolution in *Ws*, and that the results are dependent on the quantity and quality of the data and accuracy of the model parameterizations employed (Lynch and Agrawal, 1991; Lynch *et al*., 1994; Fain *et al*., 2001). Lynch and Agrawal (1991) used least-squares theory to qualitatively estimate the impact of observational noise on a model-based SPM decomposition. They demonstrated how s and vertical locations (z_i) of the backscatter data interact to influence uncertainty in the results of a model-based SPM decomposition. Rapid-settling SPM presents a difficult case for the model-dependent SPM decomposition in cases where near-bed data are limited, because most of this material is located in the near-bed region (**Figure 13**). Near the bed, the C of these particles may be readily estimated, even if the observational s is large (in absolute terms). Far from the bed, rapid-settling particles are found in such low quantities that noise in the data can easily overcome the ability of a SPM decomposition to reliably identify them. Conversely, if there are no data outside the near-bed region, then it can be difficult to resolve the slow-settling Ws-classes accurately (Lynch and Agrawal, 1991).

We used a Monte Carlo randomization approach (Manly, 1997) to quantify how uncertainties propagate through the calibration. This approach involved (a) perturbing the mean values of the major parameters (U_*, C_{OBS}, C_{ABS}, and $C_{watersample}$) with normally distributed random noise with the s values shown in **Table 2**, column 2; (b) repeating the least-squares analysis to solve eqs. (3)-(4) using the perturbed data, and adding the perturbed results to a table; (c) repeating steps a-b until the s of the tabulated results converges. Convergence was tested using a jackknife approach, where rows were systematically removed from the table in several different configurations, and the resulting estimates of s were compared. Systematic errors map directly to Ws, instead of as uncertainty in the results of the model-dependent decomposition ($C'_{a,j}$). This occurs because systematic errors contribute a uniform bias to all profiles, equivalent to a change in the value of *Ws* for a given *Ws*-class. Sources of systematic uncertainty are shown in **Figure 14**, and include the turbulent length scale (L) in eq. (6) and the diffusivity coefficient (b_j) in eq. (12). The uncertainty in *Ws* was estimated using the Monte Carlo approach described above.

We estimated parameter and observation s (**Table 2**, column 2) using targeted sampling strategies. The sampling mean s for C_{OBS} (3.5%) was estimated using periods where the sensor was held steady at depth. The sampling mean s for C_{ABS} (3.2%) and U_* (3.6%) were estimated from a single-ping data set (no averaging prior to data archiving). The eddy diffusivity for sediment ($K_{s,j}$) is represented with the shear velocity (U_*) in the uncertainty analysis. Shear velocity is a function of (and therefore represents uncertainty in) u_{300} and $c_{D,300}$. Uncertainty in the stratification parameters, *Ri*, *R* and *s*, was found to have very little impact on the calibration results for the low levels of stratification present here, so it is not included in the table. Using replicate samples, the s in $C_{watersample}$ was estimated to be 20% for surface samples, and 40% for near-bed samples.

The resulting estimates of uncertainty in $C'_{a,j}$, C''_j, g_j, and Ws_j are shown in **Table 2**, columns 3-5. The s in the results of Step 2 was 15-23% for $C'_{a,j}$, with the largest uncertainties for the fast-settling *Ws*-class. The s in the sensor bias calibration slopes was 21-41%, and the uncertainty in C''_j was from 32-48%. The s in each of the settling velocity class center-points (Ws_j) was 37%. These uncertainties were primarily a result of poor near-bed data coverage and uncertainty in $C_{watersample}$ estimates. Near-bed coverage had a large impact on the ABS analysis (and C''_3 results) because there were no ABS data near the bed; the C_{ABS} s (3.2%) was amplified in $C'_{a,2}$ and $C'_{a,3}$ (**Table 2**, row 2). There were usually more near-bed C_{OBS} data, so the higher s for C_{OBS} (5.1%) was not amplified as much in these *Ws*-classes (row 1). Using the Lynch and Agrawal (1991) method with our C_{ABS} s estimate (3.2%), we found that the s values for $C'_{a,2}$ and $C'_{a,3}$ would have been roughly halved if there were data down to the bottom grid point, at $z = 0.25$ m. The weighting of Step 2 was partially responsible for the amplification of sampling uncertainty in these results, because it reduced the influence of data points far from the bed and increased the sensitivity of the analysis to a small number of near-bed data points. As discussed in **Section 5.1**, this weighting was necessary to focus the decomposition on the region where the model was most appropriate.

6. Discussion

We briefly discuss the Fraser calibration results and ground-truth, then more broadly consider optimization, advantages, disadvantages, and future improvements of the multi-class SPM calibration approach. With respect to the results for T192 and T193, fluxes of total SPM monitored by OBS (C_{OBS}), ABS (C_{ABS}) and the multi-class SPM calibration ($\Sigma C''_j$) agreed within 40% at all depths (**Figure 11**). This suggests that these three calibration approaches all provide reasonable rough estimates of flux (or total C) in two regions with sharp differences in SPM composition. The $\Sigma C''_j$ flux estimate generally lies between the OBS and ABS estimates. This optimized estimate should be the most accurate of the three because it utilizes the best sensing capabilities of optics and acoustics, and accounts for the size-dependent bias of both sensors.

An important issue in evaluating these results is the omission of the advection term in the decomposition model, which may bias C''_j and flux estimates far from the bed. Rapid horizontal gradients in bedform characteristics and velocity along T193 (**Figure 6**), in conjunction with strong ebb currents, leads to a substantial advection term ($u\ \partial C/\partial x$) in the outer part of the water column (**Figure 12**). The mouth of the Fraser is, as a result, a challenging site to apply our calibration without including advection. We are developing a method in which transect data can be used to incorporate advection into the multi-class SPM calibration. However, most of the transects used in the calibration had a smaller advection term, and our current methodology using the simple model in eq. (2) should be sufficient for a large part of the water column.

Ground-truth data play an important role in the multi-class SPM calibration. The use of $C_{watersample}$ data in Steps 1 and 3 of the calibration assures that the resulting estimates of C''_j are reasonable. To further verify the results, relative concentrations from the multi-class SPM calibration were compared with those estimated from LISST size spectra in **Table 3**. These *Ws*-class partitioned concentration data are normalized by the total SPM concentration, and the high-resolution LISST data were bin-summed into three *Ws*-classes using the *Ws*-class divisions shown in **Table 1**. For cases where LISST size spectrum has an unresolved peak going offscale beyond the size range maximum of 500 μm, only C_1 and C_2 were compared, and these were normalized by C_1+C_2.

The correspondence between *C* data from the multi-class calibration and LISST *in situ* observations was generally good for near-bed data, but weakened with height above the bed. Near-bed relative concentration differences in about half the profiles were 0-0.04, while the profiles with the poorest agreement were typically off by as much as 0.25-0.35. The weakening relationship in the outer water column was likely a result of advection, as mentioned above. Another possible source of discrepancies arises from assumptions regarding aggregates that were used when translating the LISST data from *D* and volume concentration to *Ws* and mass concentration. We have relied on the negligible aggregation assumption (**Section 4.1**). If even a small mass of aggregates is misrepresented as primary particles, it can create errors in the estimated *Ws*-spectrum, because the difference between density (and *Ws*) of aggregates and primary particles is large.

6.1. Optimizing a planned calibration

Sampling and calibration strategies can be chosen to minimize calibration uncertainty. The calibration uncertainty is affected by factors such as the number and choice of *Ws*-classes and sensors, the sampling characteristics, and the quantity and quality of $C_{watersample}$ data. Ideally, Step 2 should involve as many *Ws*-classes as possible, to increase the resolution of the results in *Ws*-space. However, when too many *Ws*-classes are used, Step 2 results frequently contain zero-concentration values for some of the *Ws*-classes. Such results are spiky and unstable. The optimal number of *Ws*-classes, therefore, is the number of *Ws*-classes that can reliably be identified (without frequent zeros) in SPM profiles comprising a large number of *Ws*-classes. Lynch and Agrawal (1991) used the condition number of the inversion kernel G_{ij} to demonstrate that the maximum number of Ws-classes is governed by the dynamic range in z_i and the noise in the data. To clarify and elaborate upon their results, we experimented with synthetic SPM profile data and artificial noise. **Figure 15** shows contours of the number of Ws-classes identified in simulations when Step 2 is applied to synthetic C profiles consisting of twelve Ws-classes of SPM. Artificial SPM profile data used in the simulations were created based on theory presented in eq. (2), with a constant depth and U_*. One thousand SPM profiles with differing normally distributed random noise were created for each combination of s and m (the number of grid points in z_i). A number of Ws-classes were identified for each profile using the Step 2 methodology. This number was tallied for all thousand results, and the mean is contoured as the optimal number of Ws-classes.

Figure 15a shows the optimal number of Ws-classes for the sampling characteristics of our study (shaded box), where three Ws-classes appear to have been appropriate. In some cases, an instrument may not have enough vertical data points to resolve even two Ws-classes because the number of constraints on the least-squares solution is near the number of degrees of freedom. This was the case for a 300 kHz ADCP that was also used during the 2000 expedition; when the water column depth dropped below 8 m, less than 4 bins of data were available. In the other extreme, **Figure 15b** shows that it is possible to resolve eight or more Ws-classes with high resolution, near-bed data, and a range in z_i such that the regression does not need to be weighted.

Though the calibration can be utilized for a single sensor, its performance can be improved using multiple sensors. An optical sensor is vital because optics can detect a wider range of common marine particle sizes than an acoustic sensor. However, a single optical sensor is not optimal for cases with a wide range of particle sizes, because the strong response to fine sediments tends to mask the weaker response to coarse sediments. Multiple optical sensors with different wavelengths could potentially be used (Hatcher *et al*., 2000) to improve size resolution. Acoustic sensors are more attractive for monitoring coarse sediments, however, because the dependence of ABS on particle size is not strong for large particle sizes that are in the geometric scattering regime (Clay and Medwin, 1977). If an acoustic sensor is employed, it is best to utilize a vertical-beam profiler, because this eliminates the loss of data near boundaries due to side-lobe reflection. For environments with a broad range of sediment sizes, a combination of optics and acoustic sensors is generally beneficial.

The tradeoff between data uncertainty and horizontal (or temporal) resolution is a critical aspect of a sampling plan. In our study, large bedforms made it necessary to average data over distances as large as 90 m for some locations. The variance in C_{ABS}, C_{OBS} and velocity was moderate due to the moving-vessel sampling approach and high spatial variability. OBS data were averages of ~30 samples, leading to $s \approx 5.1\%$. Acoustic data were averages of ~60 samples, with $s \approx 3.2\%$. While collection of a time-series at a single location with substantial averaging (5-10 min) would have improved the quality of the data and calibration, this improvement would come at a high cost – the loss of spatial information useful for averaging over bedforms and understanding spatial variations in SPM concentration and transport.

The quantity and quality of $C_{watersample}$ data are very important, as these are used to constrain the calibration. The uncertainty in our Fraser $C_{watersample}$ data was responsible for a substantial part of our total g_j and C'' uncertainty. By collecting more samples and better $C_{watersample}$ data, this uncertainty could have been reduced substantially. Large-volume water sampling techniques, in existence for decades, are best for minimizing uncertainty associated with these samples, and a detailed error analysis with blanks and replicates is also useful.

6.2. Advantages of the multi-class SPM calibration

Advantages of our calibration approach include its high vertical and temporal (or spatial) resolution, non-intrusive nature, applicability under conditions of high shear and turbulence, and general applicability to wave-current boundary layers. Another major advantage is the fact that the analysis is defined in terms of *Ws*, not *D*; *Ws* is a critical determinant of SPM dynamics. It is better to avoid using *D* as an intermediary for *Ws,* because uncertainty in *D* is amplified in the conversion to *Ws* for fine sands and finer sediments (Gibbs et al., 1971)**.** If aggregates are present, *Ws* can also be difficult to calculate from *D*. While some approaches rely on acoustic and optical scattering theory, our method does not, thus avoiding assumptions regarding aggregate shape and density.

Another benefit is that a broad range of suspended sediment *Ws*-classes can be monitored. While any given acoustic or optical sensor can detect only a limited range of particle sizes, a very broad size range (~1 μm to ~10 mm) can be measured with a few well-chosen optical and acoustic sensors. The size range to which the method can be applied varies with flow conditions; the primary requirement is that a sediment type be suspended in large enough quantities for backscatter sensors to monitor it at the depths of data collection.

Our approach also provides an objective framework for combining the advantages of optical sensors, useful for studies of fine sediments and underwater visibility (Bunt *et al*., 1999), and acoustic sensors, useful for studies of coarse sediments, bed characteristics, bedload transport, and bedform migration (Thorne and Hanes, 2002). Few objective methodologies for a combination of this sort exist. Green *et al*. (2000) provides an approach for estimating *C* in two size classes using ABS and OBS sensors to monitor sand and silt sediment classes, respectively. This two-component approach was useful in a tide-dominated estuary with little river input, consisting primarily of two sediment classes with little or no aggregation. However, a more general approach is needed to cope with the very broad range of sizes found in many systems, and the effects of aggregation; with eight *Ws*-classes or more possible (**Figure 15**), our calibration approach represents a large step forward for high-resolution multi-class SPM monitoring technology.

A simple analysis of the short-term fate of our three SPM classes emphasizes the importance of monitoring at least three *Ws*-classes in the Fraser. For particles of each *Ws*-

class that are exported from the estuary mouth, we calculated the distance traveled seaward while they settle out of the river plume. Typical values of plume depth (3 m), plume current velocity (2 m s^{-1}), and sub-plume velocity (~0 m s^{-1}; **Figure 6**) were used for this calculation. Prior to deposition, Ws_1 particles travel >500 m to the Strait of Georgia, Ws_2 particles travel ~150 m to the upper delta slope; Ws_3 particles travel <75 m, and are retained in the estuary or at the estuary mouth. The Ws_2 sediments likely comprise fine sands and large aggregates with *Ws* between 2.5 and 18 mm s^{-1} (**Table 1**). This primary fate analysis is supported by a bed sediment survey conducted in 2000, which shows that upper delta slope sediments are dominantly fine sediments and fine sands (particle diameter < 200 um). Very little research has been done on sediment export to the delta, and most studies have simply divided SPM data into two size-classes, bed material load and washload (NHC, 1999). The utility of the decomposition of *C* into several *Ws*-classes becomes clear at this point, as a two-component approach would not provide information on the intermediate *Ws*-class (C''_2) that dominates the upper delta slope. The multi-class analysis also reveals that there is an order of magnitude cross-channel difference in export of this *Ws*-class (**Figure 11**).

This new calibration approach can help provide a large quantity of high-resolution multi-class SPM data needed for evaluating three-dimensional (3-D) models. The method can not only be applied to future SPM transport studies, but also to extensive archives of data from prior studies. It has been common for more than a decade to collect data sets including OBS, ABS, and $C_{watersample}$ measurements. If calibration uncertainty is kept within reasonable bounds, and one focuses on regions where assumptions are not violated

(**Section 5.1**), our calibrated observations are interchangeable with direct measurements of *Ws* and *C*. Furthermore, the use of data calibrated using a 1-D model is not a circular exercise, because 3-D models are forced in a fundamentally different way that the 1-D model used in the calibration, which is forced by observations.

6.3. Limitations of calibration approach

Several important qualifications must be considered when utilizing our calibration method. Foremost, the calibration employs a dynamical model that includes only vertical mixing and settling. As noted above, we are developing methods for using transect data to incorporate horizontal advection into Step 2, for cases where advection cannot be neglected. The calibration cannot be utilized without ground truth data ($C_{watersample}$), and we recommend independent verification of results using additional approaches for monitoring *Ws* and *C* (*e.g.* comparison with LISST data). Also, there is inevitably low *Ws* resolution for the finest sediments in suspension, because sediments with a wide range of *Ws* can be washload. For our Fraser calibration, with U_* up to 0.15 m s^{-1}, the washload *Ws*-class includes particles with *Ws* from ~0.01-2.5 mm s^{-1} (~1 < *D* < 60 μm). Resolution can be improved, however, with lower sampling noise (longer averaging), a higher vertical sampling density and dynamic range, and more *Ws*-classes.

Furthermore, aggregation may complicate the interpretation of results. Estimating sediment particle characteristics within a given *Ws*-class is difficult when aggregates are present, because aggregates can be made up of particles of many sizes, and both aggregates and primary particles may be present within a *Ws*-class. Also, problems can arise because size-bias is corrected in Step 3 by applying separate calibration slopes to each *Ws*-class; this implicitly assumes that *Ws* is a function of *D*. This assumption may be inaccurate if aggregates are present, leading to variability in the sensor bias calibration slopes (g_j). A solution for this problem is to perform separate calibrations for different regions and conditions. For example, a separate calibration can be made for saline waters, where aggregates are more common. One can facilitate the use of multiple calibrations by collecting a large quantity of $C_{watersample}$ data. Additionally, one could use *in situ* particle density estimates to study how g_j in these multiple calibrations varies with the profile-mean particle density. While it is difficult to measure particle density *in situ*, particularly at high resolution, it might be possible to use an aggregation model to augment this analysis.

7. Conclusions

We have presented a new calibration approach useful for monitoring suspended particulate matter (SPM) concentration in bottom boundary layers. The output of the calibration is "multi-class" SPM concentration data – concentrations in several discrete settling velocity (*Ws*) classes. The calibration is dependent upon a dynamical vertical SPM model and requires *in situ* concentration ($C_{watersample}$) data and backscatter (or transmission) from one or more acoustic or optical sensors. It is generally applicable in wave-current boundary layers, though this paper was focused on cases with currents only. The incorporation of $C_{watersample}$ data in two stages of the procedure guarantees that the resulting concentration estimates are reasonable.

An application to Fraser River estuary greater-ebb SPM export events was used to demonstrate the method, and results were compared to *in situ* particle size spectra obtained with a LISST. There was good agreement between the calibration output and LISST observations near the bed, but discrepancies increasing with height above the bed, likely due to violation of model assumptions in the outer water column. Detailed uncertainty analyses indicated that uncertainty in resulting concentration data was from 32-48%, primarily due to poor near-bed data coverage and uncertainty in $C_{watersample}$. This degree of uncertainty is not atypical for remote sediment measurement techniques. Optimized sampling strategies were presented that can dramatically reduce uncertainty for future sampling efforts.

The advantages of this method include its insensitivity to sediment size variations, wide particle size detection range, high vertical and temporal (or spatial) resolution, applicability in the presence of extreme shear or turbulence, non-intrusive nature, and the lack of assumptions on aggregate shape and/or density. Simulations suggest that the method can resolve eight *Ws*-classes or more, using common high-resolution sensors and substantial averaging to minimize noise. Three to four *Ws*-classes are more typical for measurements from a moving vessel, however. No other multi-class SPM monitoring approach has the same combination of positive attributes, including bulk calibrations, *in situ* settling chambers, underwater video, multi-frequency backscatter techniques, or laser-diffraction methods (LISST).

There are important limitations to the calibration. Foremost, the calibration employs a dynamical model that includes only vertical mixing and settling. We are studying methods for using transect data to incorporate horizontal advection into the calibration, for cases where advection cannot be neglected. Calibration slopes may vary with the proportion of aggregates. Thus, if aggregates make up a significant percentage of the suspension, one may need to stratify the optical and acoustic data in space or time, providing separate calibrations for each group of data. Water sample data are necessary as ground-truth, and one should collect at minimum, dozens, and ideally, hundreds of these samples.

Our calibrated observations are interchangeable with direct observations, as long as calibration uncertainty is kept within reasonable bounds and one focuses on regions where assumptions are not violated. Thus, the method could provide high-resolution, synoptic, spatially distributed multi-class SPM observations useful for evaluating the planned community coastal SPM transport model (Sherwood *et al.*, 2002) or other three-dimensional (3-D) models. With the basic framework presented in this paper, this new calibration approach represents a large step forward for our ability to monitor and understand multi-class SPM transport.

8. Symbols

ABS	acoustic backscatter (abbreviation)
C	SPM concentration, from bulk calibration

C'_j	SPM concentration, after model-based decomposition
C''_j	multi-class SPM concentration, after sensor bias correction
$C_{a,j}$	SPM reference concentration at $z = z_a$ (eq. 2)
C_{ABS}	concentration as measured by ABS
$c_{D,b}$	quadratic drag coefficient for reference level $z = b$ (eq. 8)
C	SPM concentration
C_j	SPM concentration for Ws-class j
C_{OBS}	concentration as measured by OBS
$C_{watersample,k}$	*in situ* estimate of concentration, $C_{watersample,k}$ [k=(1,p)]
D	SPM particle diameter
g	gravitational acceleration, 9.81 m s^{-1}
G_{ij}	inversion kernel
h	total water depth
H_{bf}	bedform height (eq. 9)
i, j, k	indices in z_i [i=(1,m)], Ws_j [j=(1,n)], and $C_{watersample,k}$ [k=(1,p)]
k_N	apparent Nikuradse roughness length (eq. 8)
K_0	neutral eddy diffusivity (eq. 6)
K_m	stratification-corrected eddy diffusivity (eq. 10)
$K_{s,j}$	mass diffusivity for sediment in Ws-class j (eq. 12)
L	length scale of the turbulent boundary layer (eq. 6)
L_{bf}	bedform wavelength (eq. 9)
m, n, p	number of data points in vectors z_i, Ws_j, and $C_{watersample,k}$
OBS	optical backscatter (abbreviation)

q	number of sensors
R	constant factor in algebraic stratification equation (eq. 10)
r^2	regression coefficient of determination
Ri	gradient Richardson number
s	constant exponent in algebraic stratification equation (eq. 10)
S	source-sink term in SPM continuity equation (eq. 1)
SPM	suspended particulate matter (abbreviation)
t	time
u	along-channel velocity in the x dimension, positive upriver
v	across-channel velocity in the y dimension
U_*	shear velocity (eq. 6)
U_b	mean velocity at height $z = b$ above the bed (eq. 7)
w	vertical velocity
Ws_j	particle settling velocity, Ws_j [$j=(1,n)$]
x	along-channel distance, upstream from Fraser buoy S0
y	across-channel distance
z	height above the bed, z_i [$i=(1,m)$]
z_a	reference level for the bottom boundary condition, $C_{a,j}$ (eq. 2)
z_0	apparent hydraulic roughness length (eq. 8)
b_j	proportionality coefficient between $K_{s,j}$ and K_m (eq. 13)
r	water density
g_j	sensor bias calibration slope (eq. 4)
k	von Kàrmàn’s constant

s	standard deviation
t_0	total bedstress, the sum of skin friction and form drag (eq. 7)

Acknowledgements

The authors would like to W.R. (Rocky) Geyer, Dan MacDonald, and Katie Gagnon for assistance during the 1999 and 2000 field efforts. Thanks also to Denise Reed for sharing her Coulter Counter, settling tube, and aggregation index results. Data collection for 1999 was funded by the National Science Foundation Land-Margin Ecosystem Research Program. Data collection for 2000 was funded by Office of Naval Research grants N000-14-97-10134 and N000-14-97-10566. Data analyses were funded by a National Science Foundation project titled, “Suspended Particulate Dynamics in Advection-Dominated Environments.”

References

Agrawal, Y.C., Pottsmith, H.C., 2000. Instruments for particle size and settling velocity observations in sediment transport. Mar. Geol. 168 (1-4), 89-114.

Beach, R.A., Sternberg, R.W., 1988. Suspended sediment transport in the surf zone: response to cross-shore infragravity motion. Mar. Geol. (80), 61-79.

Bunt, J.A.C., Larcombe, P., Jago, C.F., 1999. Quantifying the response of optical backscatter devices and transmissometers to variations in suspended particulate matter. Contin. Shelf Res. 19, 1199-1220.

Chriss, T.M., Caldwell, D.R., 1982. Evidence for the influence of form drag on bottom boundary layer flow. J. Geophys. Res. 87 (C6), 4148-4154.

Clay, C.S., Medwin, H., 1977. Acoustical Oceanography, Principles and Applications. John Wiley and Sons, New York.

Dade, W. B., Hogg, A.J., Boudreau, B.P., 2001. Physics of flow above the sediment-water interface. In: Boudreau, B.P., Jørgensen, B.B. (Eds.), The Benthic Boundary Layer. Oxford University Press, Oxford, pp. 4-43.

Davies, A.G., van de Graaff, J., Ribberink, J.S., van Rijn, L.C., Damgaard, J.S., 2002. Intercomparison of research and practical sand transport models. Coastal Engin. 46 (1), 1-23.

Deines, K. L., 1999. BBADCP- Backscatter estimation using broadband acoustic Doppler current pro-filers. In: Anderson, S. P., Terray, E.A., Rizzoli White, J. A., Williams, A. J. III (Eds.), Proceedings of the IEEE Sixth Working Conference on Current Measurement, pp. 258-263.

Dyer, K.R., 1986. Coastal and Estuarine Sediment Dynamics. Wiley-Interscience, New York.

Dyer, K.R., Manning, A.J., 1999. Observation of the size, settling velocity and effective density of flocs, and their fractal dimensions. J. Sea Res. 41, 87-95.

Dyer, K.R., Cornelisse, J., Dearnaley, M.P., Fennessy, M.J., Jones, S.E., McCave, I.N., Pejrup, M., Puls, W., van Leussen, W., Wolfstein, K., 1996. A comparison of *in situ* techniques for estuarine floc settling velocity measurement. J. Sea Res. 36, 15-29.

Fain, A.M.V., Jay, D. A., Wilson, D. J., Orton, P. M., Baptista, A. M., 2001, Seasonal, monthly and tidal patterns of particulate matter dynamics in the Columbia River estuary. Estuaries 24, 770-786.

Gibbs, R.J., Matthews, M.D., Link, D.A., 1971. The relationship between sphere size and settling velocity. J. Sed. Petrol. 41, 7-18.

Grant, W.D., Madsen, O.S., 1982. Movable bed roughness in oscillatory flow, J. Geophys. Res., 87:469.

Green, M.O., Bell, R.G., Dolphin, T.J., Swales, A., 2000. Silt and sand transport in a deep tidal channel of a large estuary (Manaku Harbour, New Zealand). Mar. Geol. 163, 217-240.

Hatcher, A., Hill, P., Grant, J., Macpherson, P., 2000. Spectral optical backscatter of sand in suspension: effects of particle size, composition, and colour. Mar. Geol. 168, 115-128.

Hill, P.S., Nowell, A.R.M., Jumars, P.A., 1988. Flume evaluation of the relationship between suspended sediment concentration and excess boundary shear stress. J. Geophys. Res. 93 (C10), 12499-12509.

Kineke, G.C., Sternberg, R.W., 1989. The effect of particle settling velocity on computed suspended sediment concentration profiles. Mar. Geol. 90, 159-174.

Kostaschuk, R.A., Luternauer, J.L., 1989. The role of the salt-wedge in sediment resuspension and deposition: Fraser River Estuary, Canada. J. Coastal Res. 5 (1), 93-101.

Kostaschuk, R.A., Ilersich, S.A., 1995. Dune geometry and sediment transport: Fraser River, British Columbia. In: Hickin, E.J. (Ed.), River Geomorphology. John Wiley & Sons, Sussex, pp. 19-36.

Lehfeldt, R., Bloss, S., 1989. Algebraic turbulence model for stratified tidal flows. In: Dronkers, J., van Leussen, W. (Eds.), Physical Processes in Estuaries. Springer Verlag, New York, pp. 347-403.

Long, C.E., 1981. A simple mathematical model for time dependent stably stratified turbulent boundary layers. Ph.D. dissertation, Dept. of Oceanography, University of Washington, Seattle, WA.

Lynch, J. F., Agrawal, Y. C., 1991. A model-dependent method for inverting vertical profiles of scattering to obtain size spectra in boundary layers. Mar. Geol. 99, 387-401.

Lynch, J.F, Irish, J.D, Sherwood, C.R., Agrawal, Y.C., 1994. Determining suspended sediment particle size information from acoustical and optical backscatter measurements. Contin. Shelf Res. 14, 1139-1165.

Macdonald, D.G., Geyer, W.R., 2002. Mixing processes and hydraulic control in a highly stratified estuary. Ph.D. dissertation, Joint Program in Oceanography / Applied Ocean Science and Engineering, Woods Hole Oceanographic Institution, Woods Hole, MA.

Manly, B.F., 1997. Randomization, Bootstrap & Monte Carlo Methods in Biology. Chapman & Hall, London.

Menke, W., 1989. Geophysical Data Analysis: Discrete Inverse Theory. Academic Press, London.

Milligan, T.G., 1995. An examination of the settling behaviour of a flocculated suspension. Neth. J. Sea Res. 33 (2), 163-171.

NHC, 1999. Lower Fraser River Sediment Budget Analysis: Final Report. Report prepared for Fraser River Estuary Management Program. Northwest Hydraulic Consultants, North Vancouver, British.Columbia.

Orton, P.M., Kineke, G.C., 2001. Comparing calculated and observed vertical suspended sediment distributions from a Hudson River Estuary turbidity maximum. Estuar. Coast. Shelf Sci. 52 (3), 401-410.

Reed, D.J., Donovan, J., 1994. The character and composition of the Columbia River estuarine turbidity maximum. In: Dyer, K., Orth, R. (Eds.), Changing Particle Fluxes in Estuaries: Implications from Science to Management, ECSA/ERF22 Symposium. Olsen & Olsen Press, Friedensborg, pp. 445-450.

Rose, C.P., Thorne, P.D., 2001. Measurements of suspended sediment transport parameters in a tidal estuary. Contin. Shelf Res. 21, 1551-1575.

Sherwood, C.R., Harris, C.K., Geyer, W.R., Butman, B., 2002. Toward a community coastal sediment-transport modeling system: report of the second workshop. EOS, Trans. Amer. Geophys. Union 83 (50), 605.

Stanton, T.K., Chu, D., Wiebe, P.H., 1998. Sound Scattering by Several Zooplankton Groups II: Scattering Models. J. Acoust. Soc. Am. 103, 236-253.

Sternberg, R.W., 1972. Predicting initial motion and bedload transport of sediment particles in the shallow marine environment. In: Swift, D.J.P., Duane, D.B., Pilkey, O.H. (Eds.), Shelf Sediment Transport: Process and Pattern. Dowden, Hutchinson and Ross, Stroudsburg, PA, pp. 61-81.

Thevenot, M.M., Kraus, N.C., 1993. Comparison of acoustical and optical measurements of suspended material in the Chesapeake Estuary. J. Marine Env. Eng. 1, 65-79.

Thorne, P.D. Hanes, D.M., 2002. A review of acoustic measurement of small-scale sediment processes. Contin. Shelf Res. 22, 603-632.

Zyserman, J.A., Fredsoe, J.,1994. Data analysis of bed concentration of suspended sediment. J. Hydraul. Eng. 120 (9), 1021–1042.

Table 1: Settling velocity classes chosen for Step 2, the model-dependent decomposition.

j **Ws-class**	**Ws (mm s^{-1})**	**Ws range (mm s^{-1})**	**Dominant Material**	**b_i from eq. (12) (for $U_* = 0.08$ m s^{-1})**
1	0.01	<2.5	fine sediments	0.62
2	10	2.5-18	120 µm sand, large aggregates	0.80
3	37	>18	sand, 300 µm	2.1

Table 2: Monte Carlo simulation results for the uncertainty analysis, *Ws*-classes *j* = 1,2,3.

row #	**Uncertainty Source (variable or row #; std. dev s)**	**Monte Carlo outcome, *j*=1 (variable; s)**	**Monte Carlo outcome, *j*=2 (variable; s)**	**Monte Carlo outcome, *j*=3 (variable; s)**
1	C_{OBS} ±5.1%	$C'_{a,1}$±15%	$C'_{a,2}$±21%	$C'_{a,3}$±24%
2	C_{ABS} ±3.2%	$C'_{a,1}$±6%	$C'_{a,2}$±22%	$C'_{a,3}$±23%
3	U_* ±3.6%	$C'_{a,1}$±2%	$C'_{a,2}$±3%	$C'_{a,3}$±3%
4	L ±~33%	Ws_1±27%	Ws_2±27%	Ws_3±27%
5	β ±~25%	Ws_1±25%	Ws_2±25%	Ws_3±25%
6[a]	#1,2,3	$C'_{a,1}$±15%	$C'_{a,2}$±21%	$C'_{a,3}$±23%
7[a,b]	#1,2,3,$C_{watersample}$ ±20-40%	γ_1±28%	γ_2±21%	γ_3±41%
8[a,b]	#1,2,3,$C_{watersample}$ ±20-40%	C''_1±35%	C''_2±32%	C''_3±48%
9[a,b]	#4,5[a]	Ws_1±37%	Ws_2±37%	Ws_3±37%

[a] For rows 6-9, uncertainty sources are combinations of the row numbers shown

[b] Rows 7-9 show final calibration uncertainties

Table 3: Comparison of SPM concentration data[a] from the multi-class calibration and LISST *in situ* observations.

Sample/ transect	h (m)	U_* (m s^{-1})	z (m)	LISST C_1	Calib. C''_1	LISST C_2	Calib. C''_2	LISST C_3	Calib. C''_3
T187-1	10	0.095	0.5	0.443	0.468	0.556	0.532	offscale	-
			4	0.654	0.561	0.346	0.439	offscale	-
T187-2	13	0.091	0.5	0.556	0.355	0.445	0.645	offscale	-
			4	0.668	0.453	0.332	0.548	offscale	-
T191	11.5	0.061	0.5	0.394	0.404	0.495	0.520	0.111	0.076
			4	0.634	0.492	0.335	0.467	0.031	0.039
T194	12	0.068	0.5	0.467	0.135	0.533	0.865	offscale	-
			4	0.609	0.191	0.391	0.809	offscale	-
T195	6	0.057	0.5	0.690	0.650	0.236	0.263	0.074	0.087
			4	0.702	0.868	0.232	0.130	0.066	0.003
T198	11	0.083	0.5	0.520	0.314	0.480	0.686	offscale	-
			4	0.561	0.384	0.439	0.606	offscale	-
upstream	10	0.026	0.5	0.452	0.485	0.457	0.515	0.091	0
anchor-1			4	0.502	0.804	0.436	0.196	0.063	0
upstream	10	0.027	0.5	0.498	0.747	0.434	0.253	0.069	0
anchor-2			4	0.519	0.897	0.433	0.104	0.048	0

[a] *Ws*-class partitioned concentration data are normalized by the total SPM concentration, or C_1+C_2 in cases where LISST C_3 is offscale.

Figure Captions

Figure 1: Diagram of the three-step multi-class SPM calibration approach for acoustic backscatter (ABS) and optical backscatter (OBS), with three *Ws*-classes. The *in situ* water sample concentration data ($C_{watersample}$) are used to constrain the calibration in Steps 1 and 3.

Figure 2: Calibration Step 2 (model-dependent decomposition; eq. 3) results for optical (left) and acoustic (right) estimates of SPM concentration (C_{OBS}, C_{ABS}). Scaled basis functions (C'_1,C'_2,C'_3) are shown for three settling velocity classes (0.01, 10, 37 mm s^{-1}). Scaling was set using a multivariate non-negative least-squares linear regression, so that their sum ($C'_1+C'_2+C'_3$) most closely approximates the total concentration estimate from Step 1 (C_{OBS} or C_{ABS}).

Figure 3: The theoretical responses of two sensors to Fraser River sediments, an optical sensor (OBS) and a 1200 kHz acoustic sensor (ABS). Fraser SPM is represented by a Coulter Counter particle size (D) distribution.

Figure 4: Fraser River entrance, with bathymetry contours in meters, based on a compilation of bathymetric data from the Canadian Hydrographic Service (Chart 3490, 1997), and shipboard measurements (July 2000). The bold dashed line represents the location of the 12 m bathymetric contour. The two dotted lines show transects T192 and T193 (adapted from MacDonald and Geyer, 2002).

Figure 5: Calibration Step 1, the total (bulk) suspended particulate matter calibrations for (left) optical backscatter (OBS), and (right) 1200 kHz acoustic backscatter (ABS) for the Fraser 2000 expedition. The OBS bulk calibration regression statistics correspond to the regression line for 0.06-0.45 V, while lower OBS responses represent a nearly constant background concentration of 35 mg l^{-1}.

Figure 6: T193 observations, from top axis down: Salinity, with a dotted line showing the instrument trackline; the optical estimate of total SPM concentration, C_{OBS}, also with trackline; the acoustic estimate of total SPM concentration, C_{ABS}; and the along-channel velocity (seaward at all points).

Figure 7: A LISST-100 *in situ* particle size spectrum from the Fraser mouth during a greater-ebb SPM export event, with estimated settling velocity (**Section 4.2.1**) on the top axis. The conversion of LISST volume concentration data to mass concentration is discussed in **Section 4.1**. At most, aggregates (dashed lines) made up only a small fraction of total freshwater SPM mass concentration during Fraser freshet conditions, according to aggregation indices (D. Reed, unpubl. data).

Figure 8: Vertical profiles of several variables from the upriver end of T193, including ebb current speed, optically-derived total concentration (C_{OBS}), Richardson number, and eddy diffusivity. Gradients in concentration lead to mild stratification that in turn lead to

reduced estimates of eddy diffusivity (K_m) below the diffusivity for a neutrally buoyant water column (K_0).

Figure 9: T193 concentration data based on the multi-class SPM calibration, from the top: C''_1, C''_2, C''_3, and a combination plot of U_* and the r^2 values for the C_{OBS} and C_{ABS} model-dependent decompositions.

Figure 10: Calibration Step 3, the sensor bias calibration. The sensor bias calibration slopes for optics, g_1 and g_2, and for acoustics, g_3, are shown on the plot. Error bars are also shown, based on estimated $C_{watersample}$ standard deviations (s) and estimates of s in $C'_{a,j}$ from row 6 of **Table 2**.

Figure 11: Seaward fluxes of SPM for T192 and T193, based on C_{OBS}, C_{ABS}, the multi-class SPM calibration sum ($\Sigma C''_j = C''_1+C''_2+C''_3$), and each separate *Ws*-class (C''_1, C''_2, C''_3).

Figure 12: Comparison of the magnitude of spatially averaged terms in the mass continuity equation (eq. 1) for T193 ($0 < x < 0.9$ km). The vertical and cross-channel advection terms (not shown) were below 0.1 mg l^{-1} s^{-1}. The discrepancy, the sum of all signed terms, indicates the size of the net error in this dynamic balance.

Figure 13: Sketch of a hypothetical data set where noise, low resolution (0.5 m), and poor near-bed data coverage lead to an erroneous result in the model-based

decomposition (Step 2). The thin-line profile and shaded population standard deviation (s) represent a noisy SPM field, while each ‘X’ represents poor-quality observational data. The bold vertical line represents a possible result where Step 2 detects washload but no fast-settling SPM.

Figure 14: The systematic uncertainty in decomposition model profile shapes for the three *Ws*-classes. The “no bias” profiles were calculated from eq. (2), with U_* = 0.10 m s^{-1}, h = 9 m, and b and L as defined in eqs. (6) and (12).

Figure 15: Contours of the optimal number of *Ws*-classes in Step 2, the model-dependent decomposition. In the left panel, we show the optimal number for the Fraser calibration. The range in number of evenly-spaced vertical grid points (m) and the optical and acoustic standard deviation (s) are marked with dashed lines and a shaded area for reference. In the right panel, it is assumed that no regression weighting is necessary and data are present throughout the water column. Details are given in **Section 6.1**.

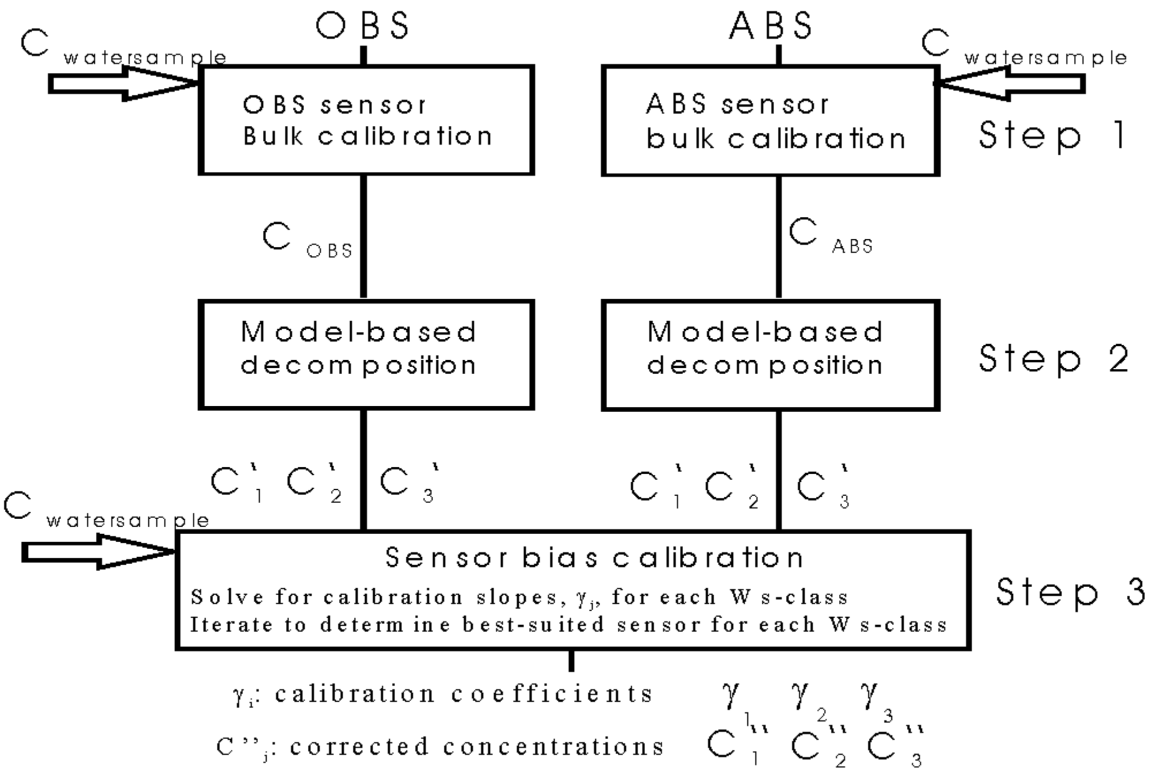

Figure 1: Diagram of the three-step multi-class SPM calibration approach for acoustic backscatter (ABS) and optical backscatter (OBS), with three *Ws*-classes. The *in situ* water sample concentration data ($C_{watersample}$) are used to constrain the calibration in Steps 1 and 3.

Figure 2, left panel

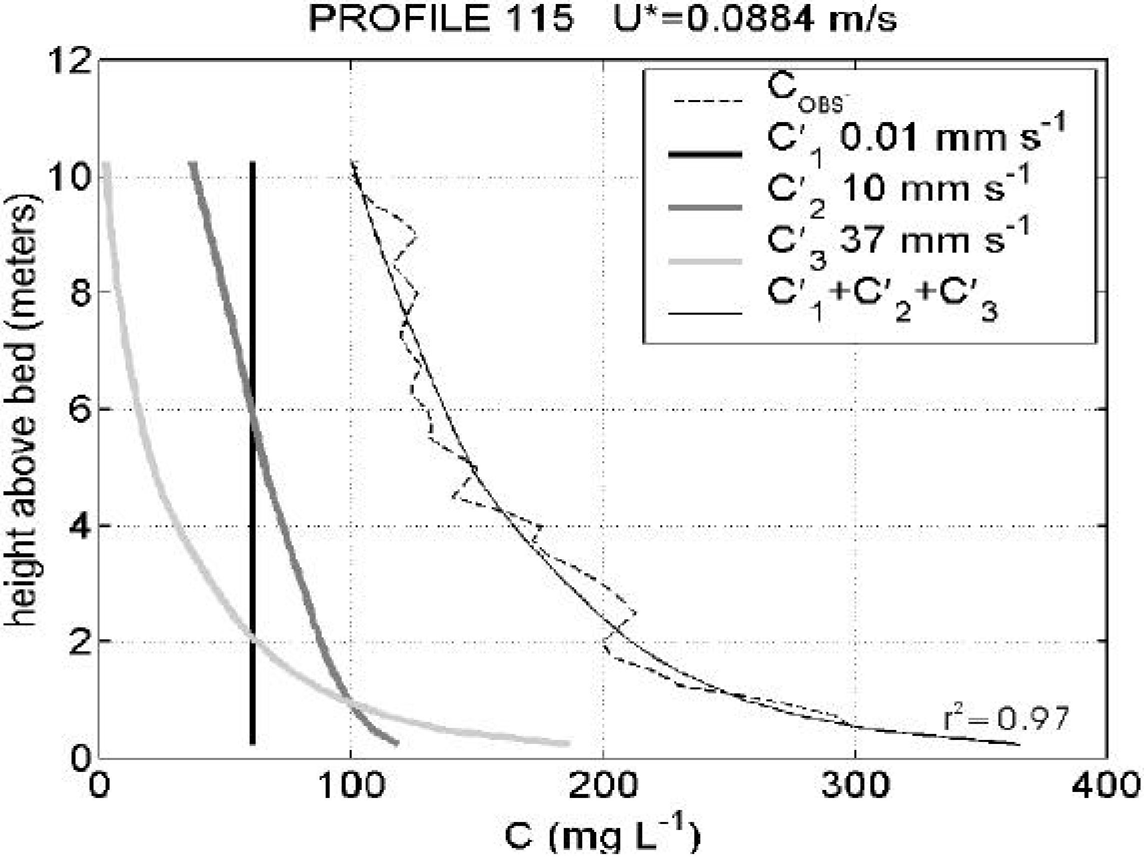

Figure 2, right panel

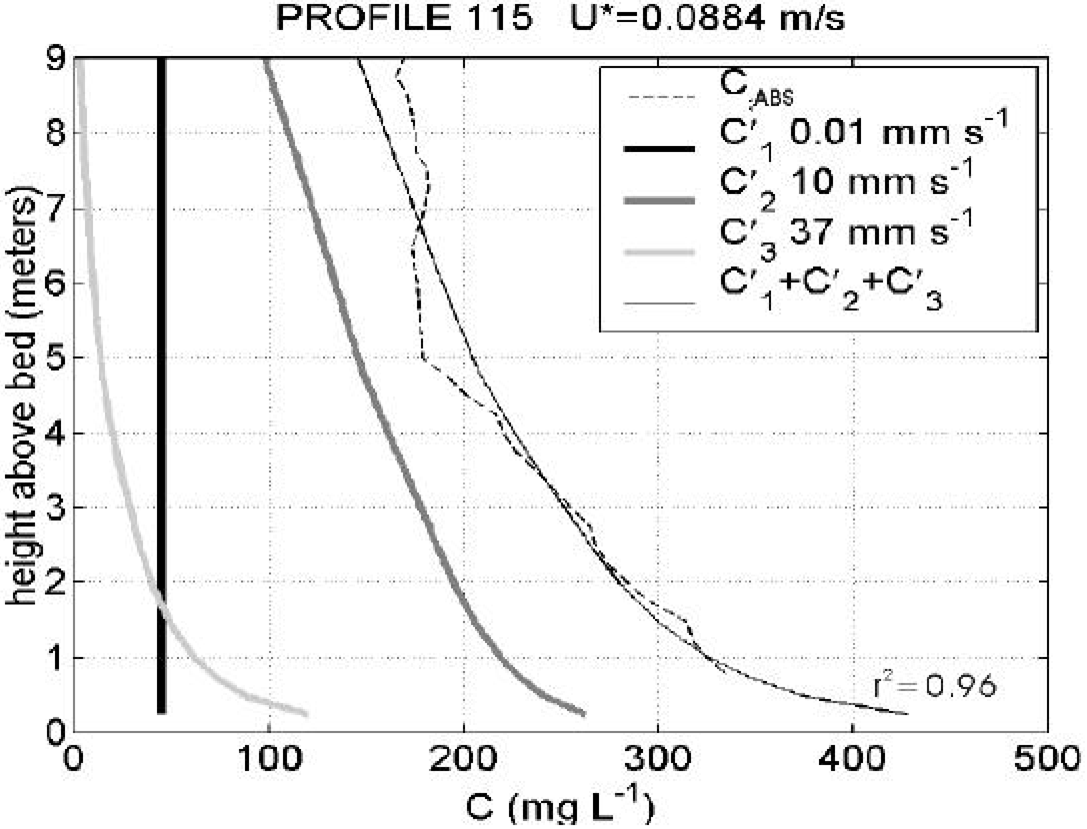

Figure 2: Calibration Step 2 (model-dependent decomposition; eq. 3) results for optical (left) and acoustic (right) estimates of SPM concentration (C_{OBS}, C_{ABS}). Scaled basis functions (C'_1,C'_2,C'_3) are shown for three settling velocity classes (0.01, 10, 37 mm s^{-1}). Scaling was set using a multivariate non-negative least-squares linear regression, so that their sum ($C'_1+C'_2+C'_3$) most closely approximates the total concentration estimate from Step 1 (C_{OBS} or C_{ABS}).

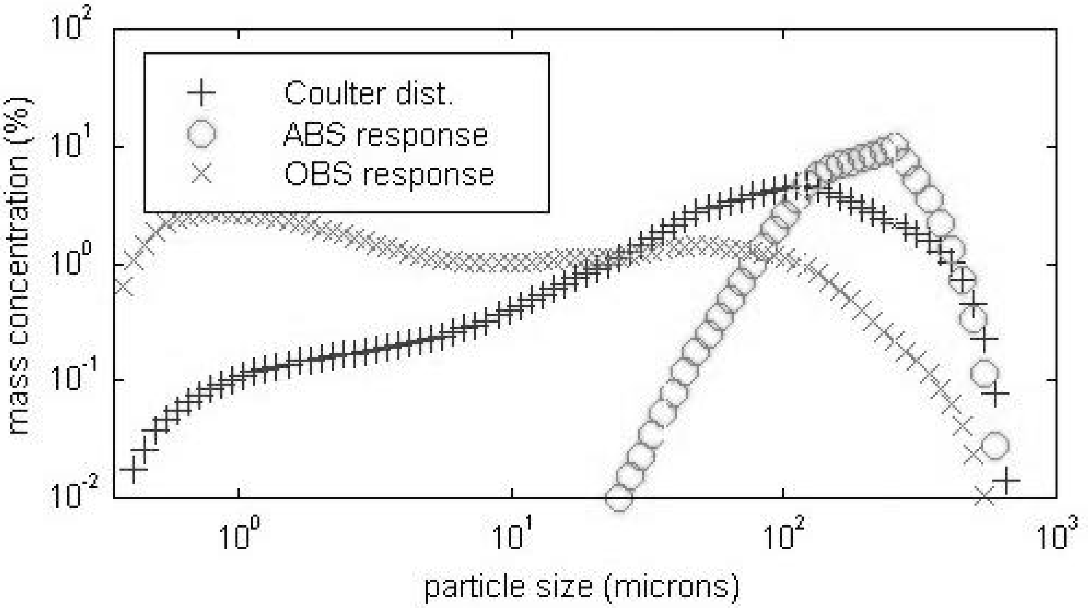

Figure 3: The theoretical responses of two sensors to Fraser River sediments, an optical sensor (OBS) and a 1200 kHz acoustic sensor (ABS). Fraser SPM is represented by a Coulter Counter particle size (*D*) distribution.

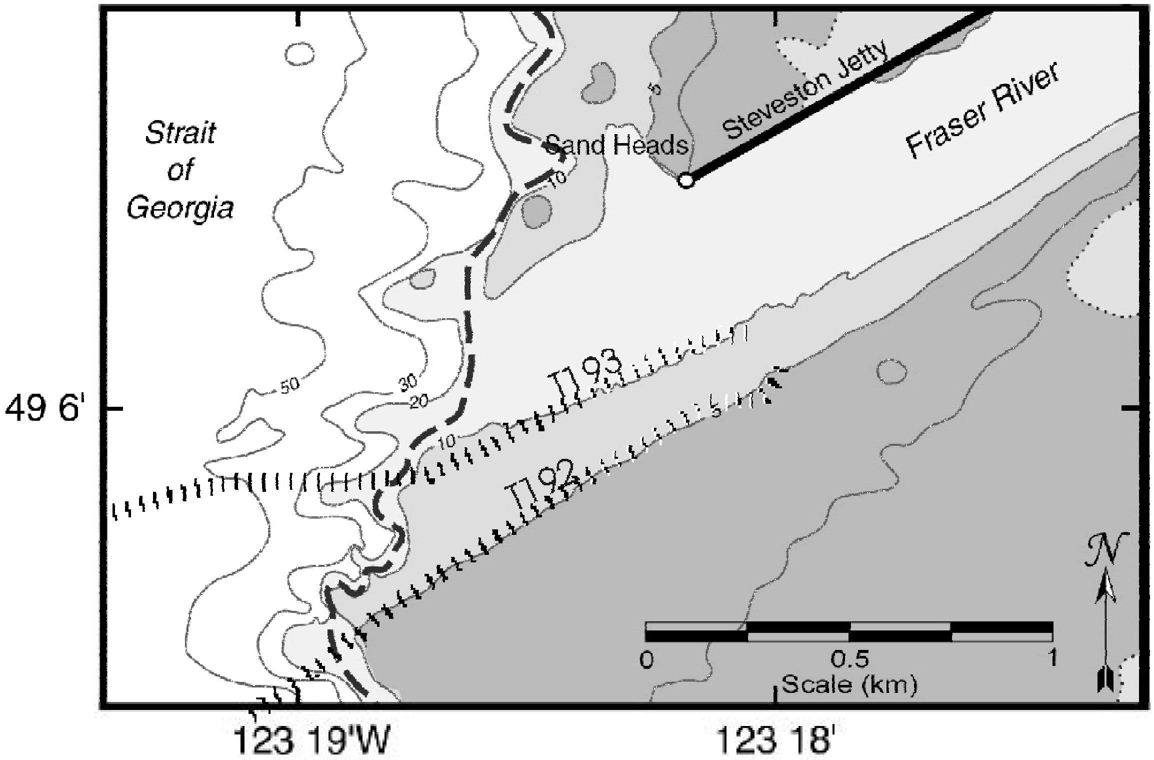

Figure 4: Fraser River entrance, with bathymetry contours in meters, based on a compilation of bathymetric data from the Canadian Hydrographic Service (Chart 3490, 1997), and shipboard measurements (July 2000). The bold dashed line represents the location of the 12 m bathymetric contour. The two dotted lines show transects T192 and T193 (adapted from MacDonald and Geyer, 2002).

Figure 5, left panel

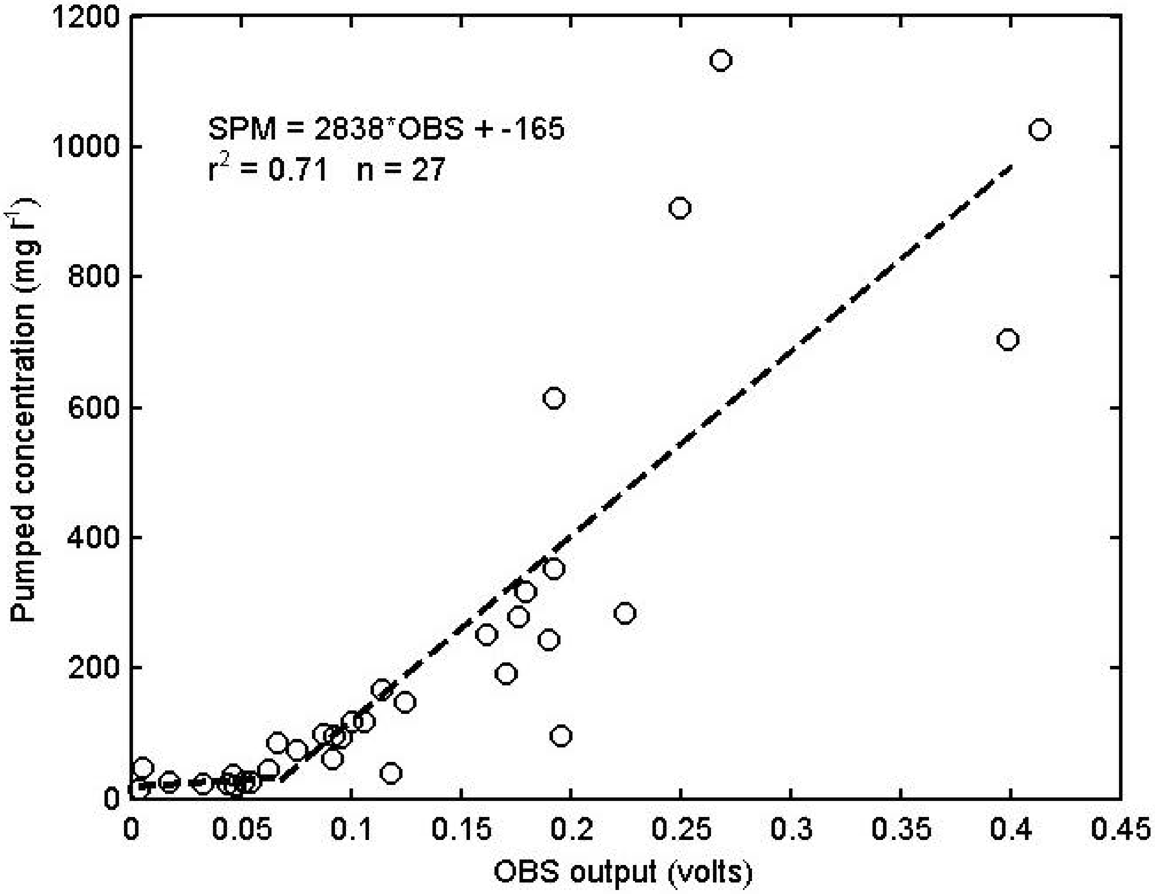

Figure 5, right panel

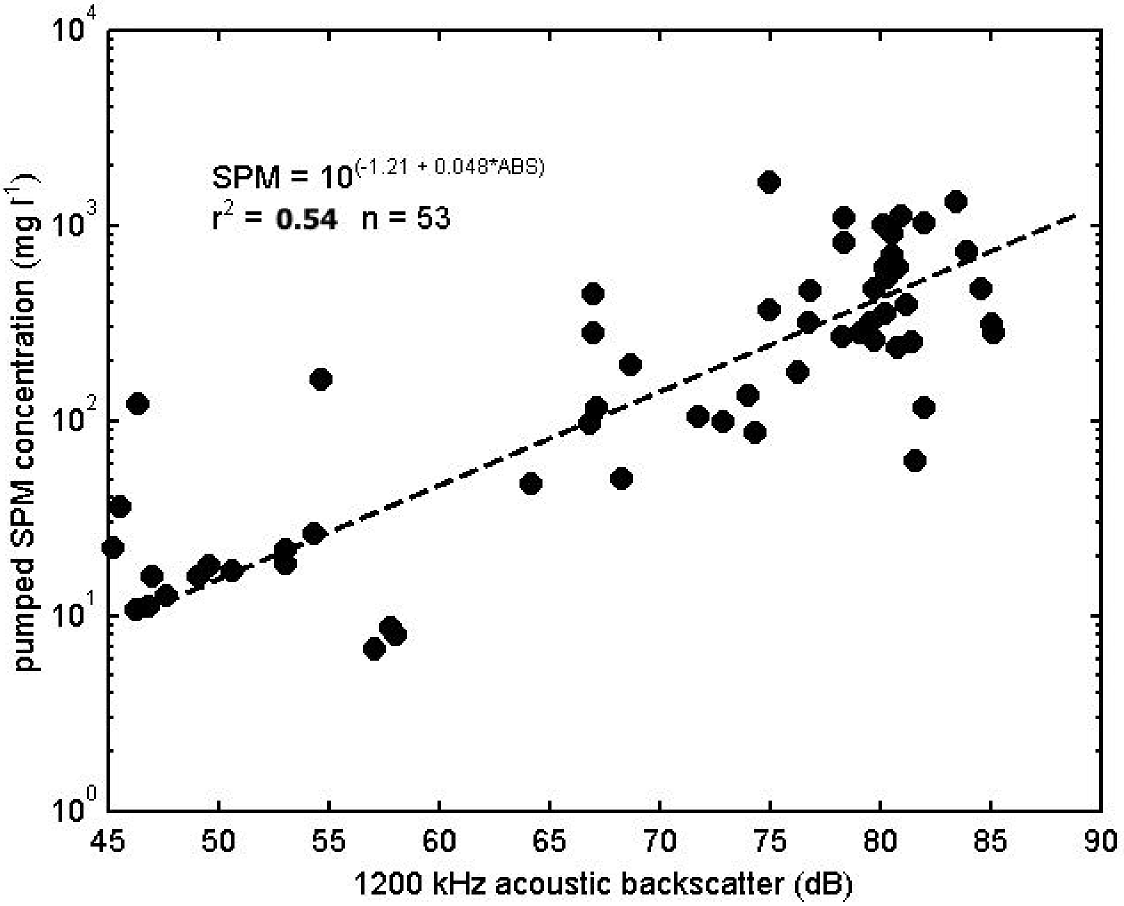

Figure 5: Calibration Step 1, the total (bulk) suspended particulate matter calibrations for (left) optical backscatter (OBS), and (right) 1200 kHz acoustic backscatter (ABS) for the Fraser 2000 expedition. The OBS bulk calibration regression statistics correspond to the regression line for 0.06-0.45 V, while lower OBS responses represent a nearly constant background concentration of 35 mg l^{-1}.

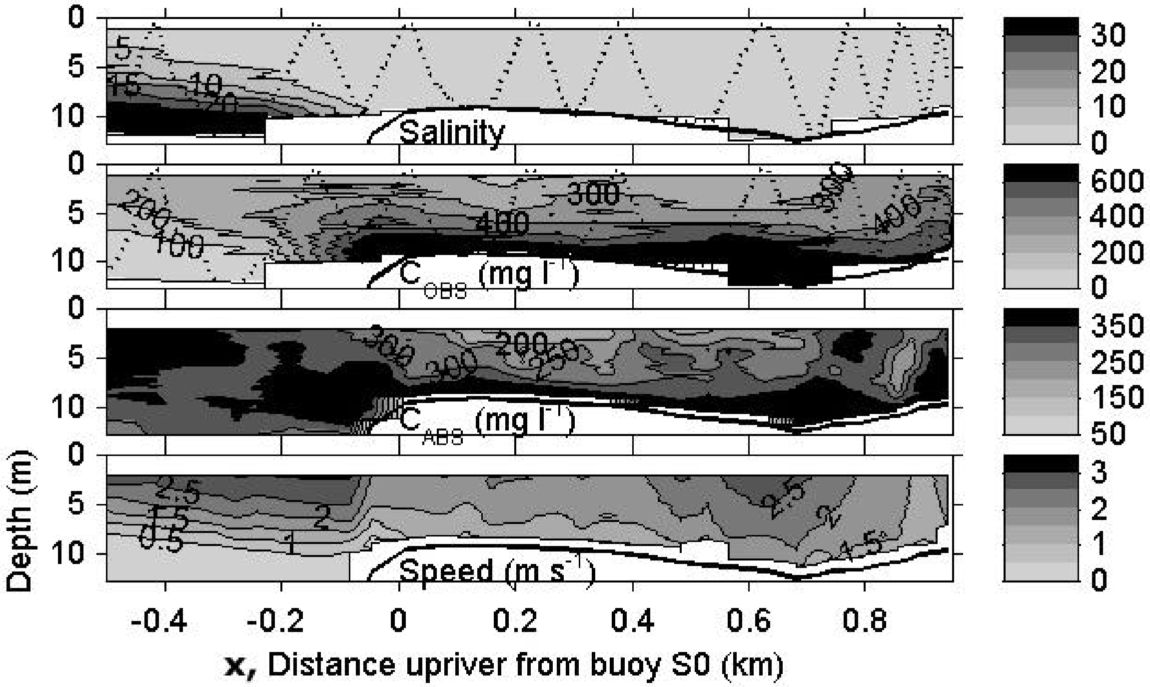

Figure 6: T193 observations, from top axis down: Salinity, with a dotted line showing the instrument trackline; the optical estimate of total SPM concentration, C_{OBS}, also with trackline; the acoustic estimate of total SPM concentration, C_{ABS}; and the along-channel velocity (seaward at all points).

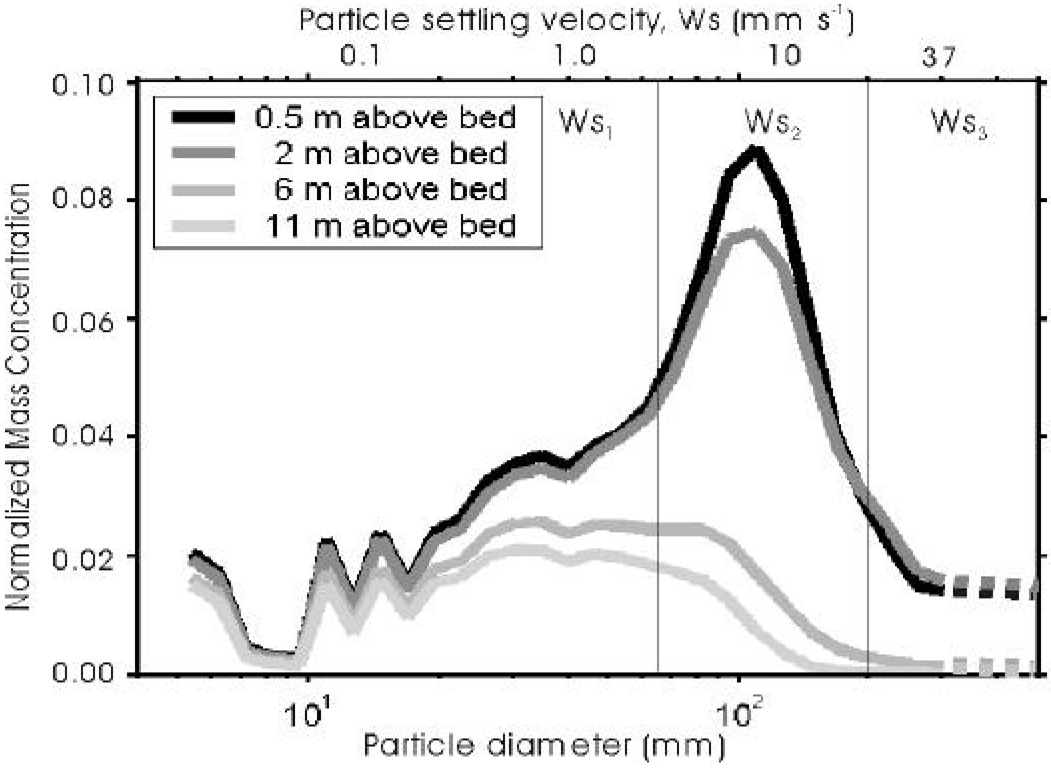

Figure 7: A LISST-100 *in situ* particle size spectrum from the Fraser mouth during a greater-ebb SPM export event, with estimated settling velocity (**Section 4.2.1**) on the top axis. The conversion of LISST volume concentration data to mass concentration is discussed in **Section 4.1**. At most, aggregates (dashed lines) made up only a small fraction of total freshwater SPM mass concentration during Fraser freshet conditions, according to aggregation indices (D. Reed, unpubl. data).

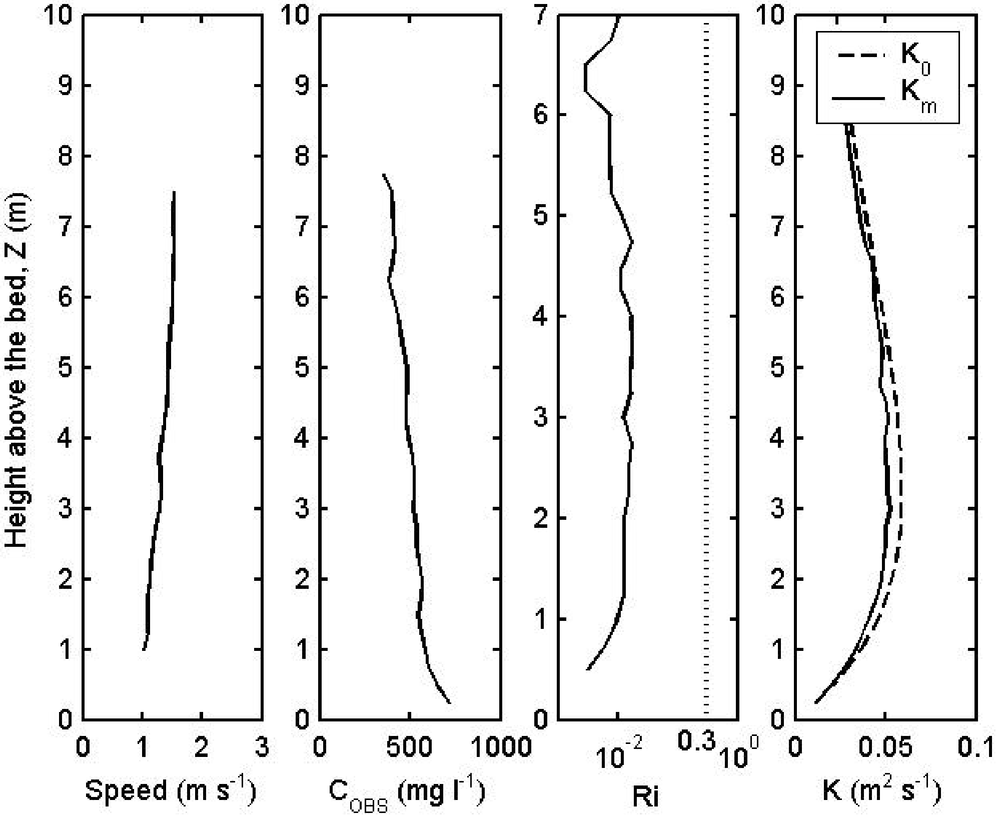

Figure 8: Vertical profiles of several variables from the upriver end of T193, including ebb current speed, optically-derived total concentration (C_{OBS}), Richardson number, and eddy diffusivity. Gradients in concentration lead to mild stratification that in turn lead to reduced estimates of eddy diffusivity (K_m) below the diffusivity for a neutrally buoyant water column (K_0).

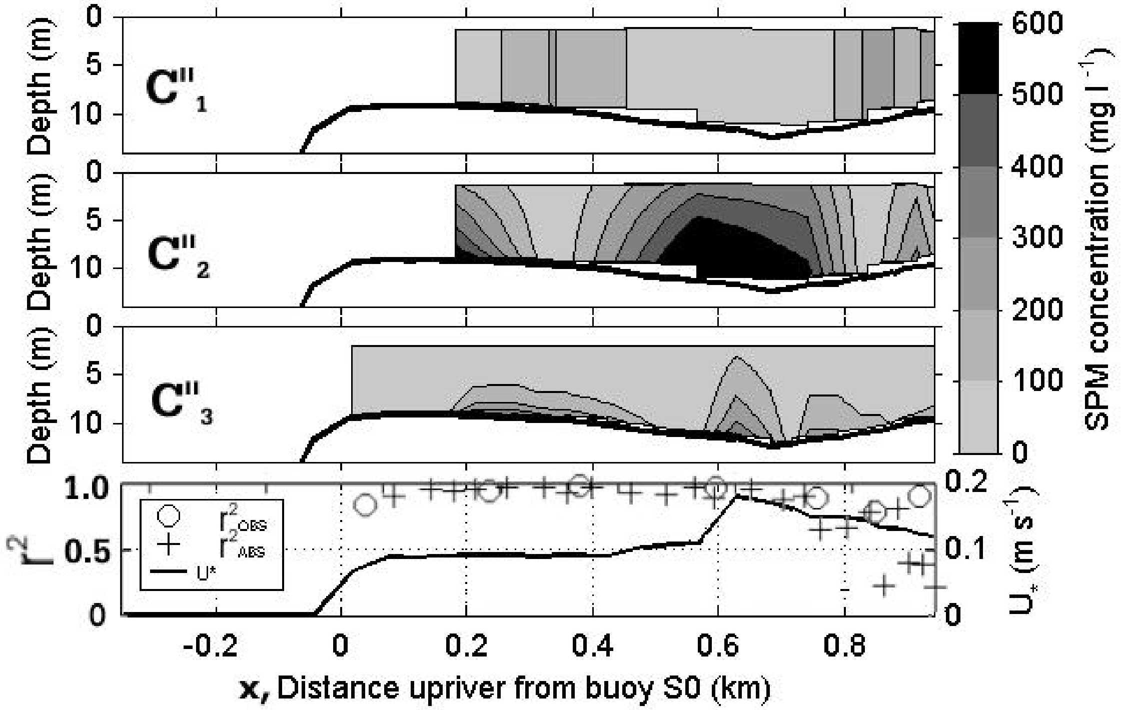

Figure 9: T193 concentration data based on the multi-class SPM calibration, from the top: C''_1, C''_2, C''_3, and a combination plot of U_* and the r^2 values for the C_{OBS} and C_{ABS} model-dependent decompositions.

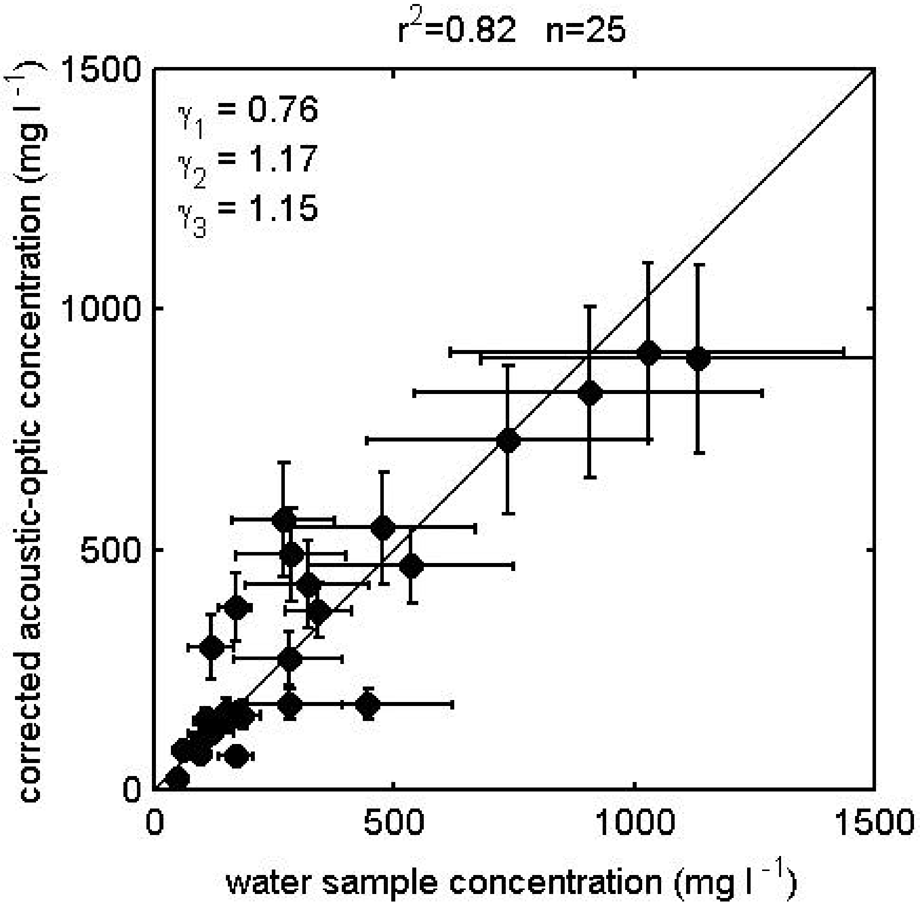

Figure 10: Calibration Step 3, the sensor bias calibration. The sensor bias calibration slopes for optics, g_1 and g_2, and for acoustics, g_3, are shown on the plot. Error bars are also shown, based on estimated $C_{watersample}$ standard deviations (s) and estimates of s in $C'_{a,j}$ from row 6 of **Table 2**.

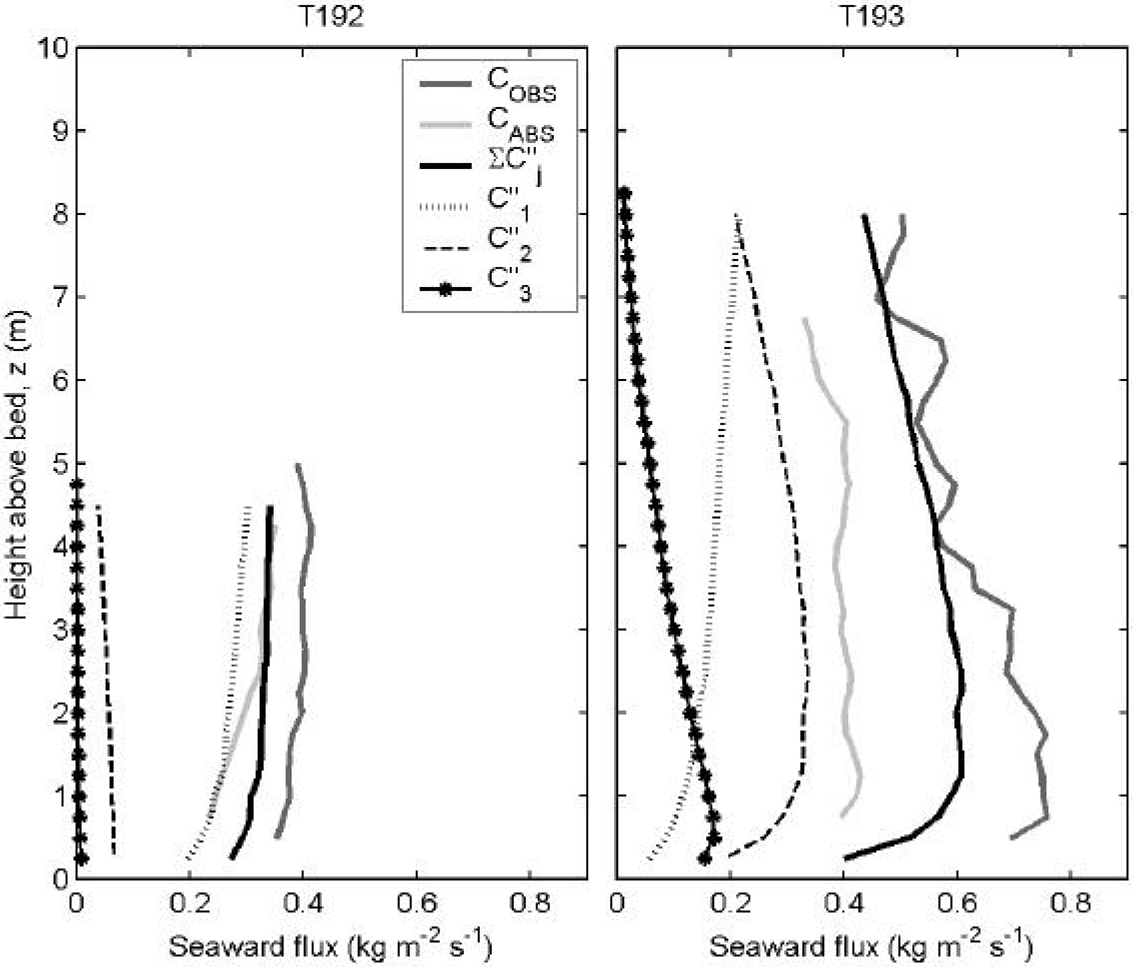

Figure 11: Seaward fluxes of SPM for T192 and T193, based on C_{OBS}, C_{ABS}, the multi-class SPM calibration sum ($\Sigma C''_j = C''_1 + C''_2 + C''_3$), and each separate *Ws*-class (C''_1, C''_2, C''_3).

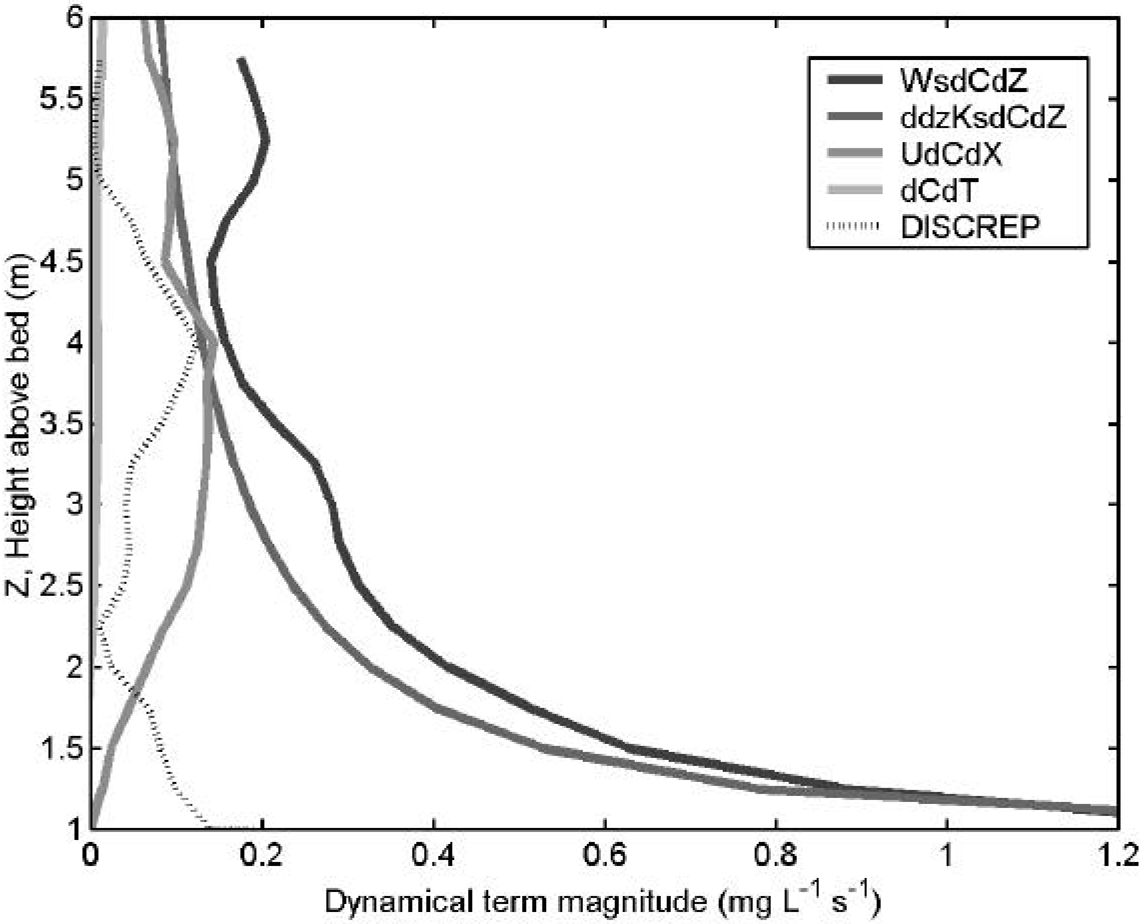

Figure 12: Comparison of the magnitude of spatially averaged terms in the mass continuity equation (eq. 1) for T193 ($0 < x < 0.9$ km). The vertical and cross-channel advection terms (not shown) were below 0.1 mg l^{-1} s^{-1}. The discrepancy, the sum of all signed terms, indicates the size of the net error in this dynamic balance.

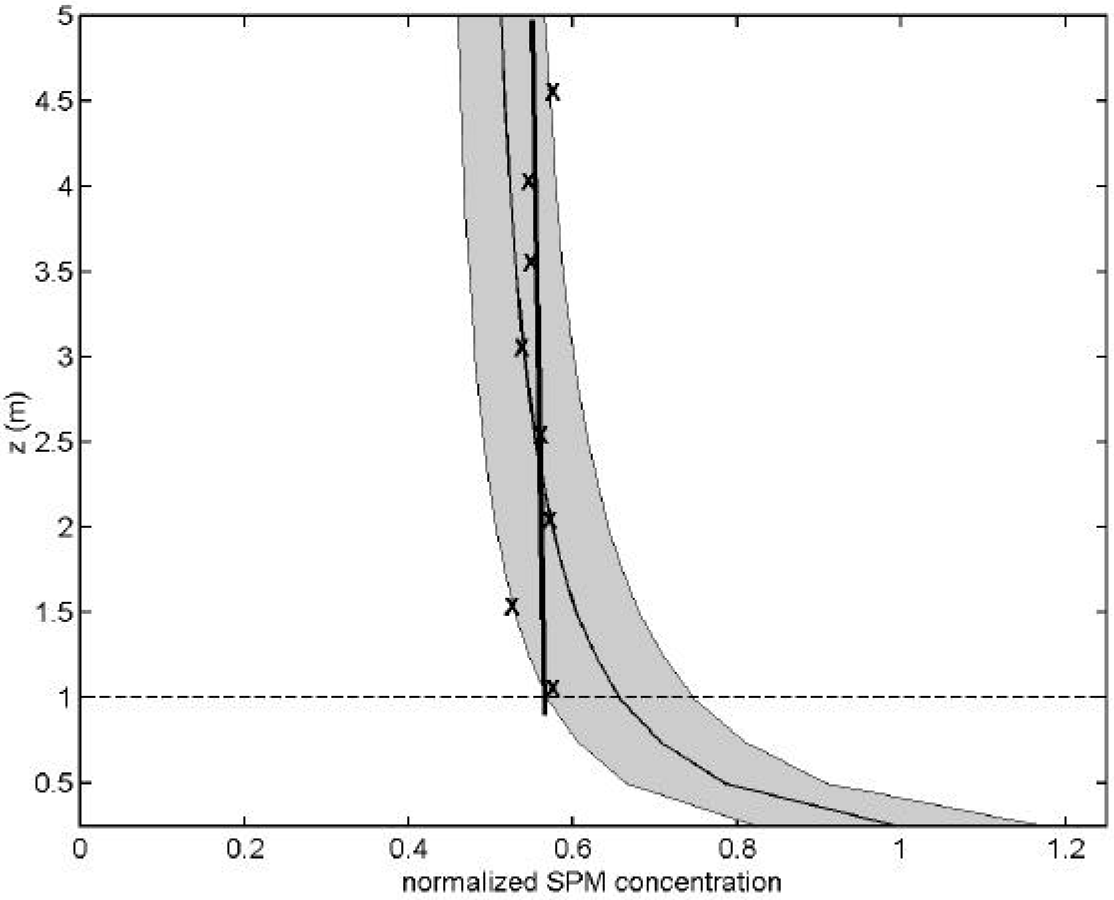

Figure 13: Sketch of a hypothetical data set where noise, low resolution (0.5 m), and poor near-bed data coverage lead to an erroneous result in the model-based decomposition (Step 2). The thin-line profile and shaded population standard deviation (s) represent a noisy SPM field, while each 'X' represents poor-quality observational data. The bold vertical line represents a possible result where Step 2 detects washload but no fast-settling SPM.

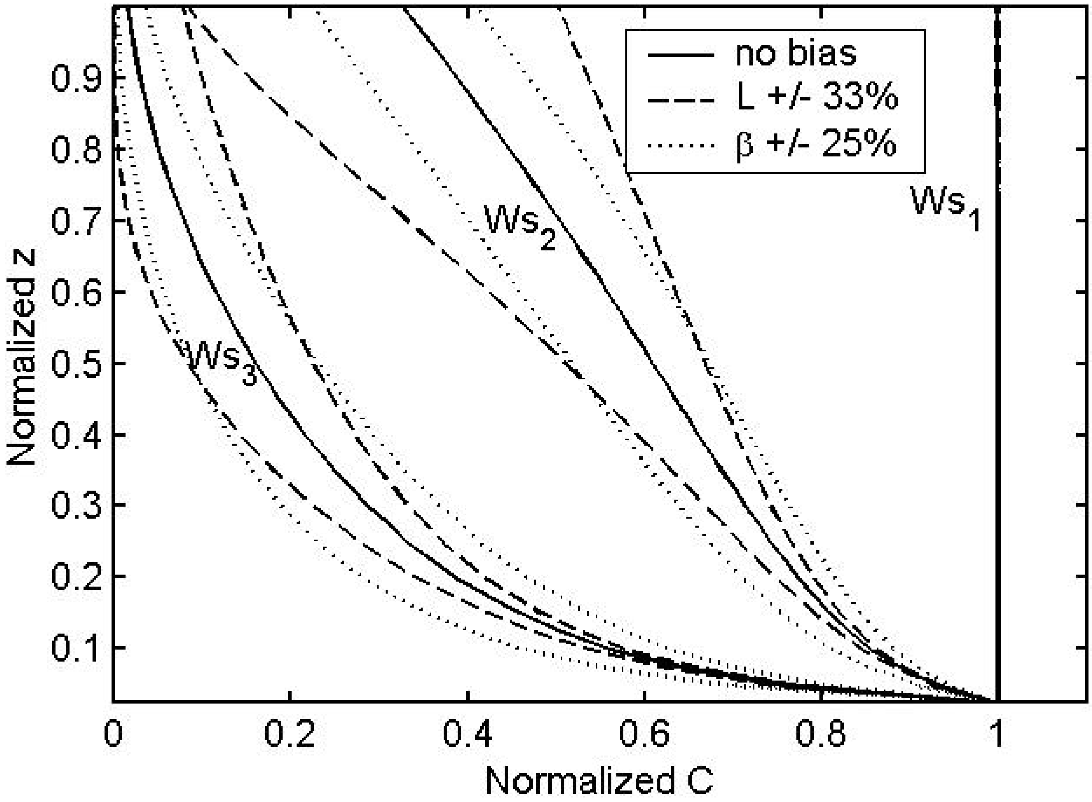

Figure 14: The systematic uncertainty in decomposition model profile shapes for the three *Ws*-classes. The "no bias" profiles were calculated from eq. (2), with U_* = 0.10 m s^{-1}, h = 9 m, and b and L as defined in eqs. (6) and (12).

Figure 15, left panel

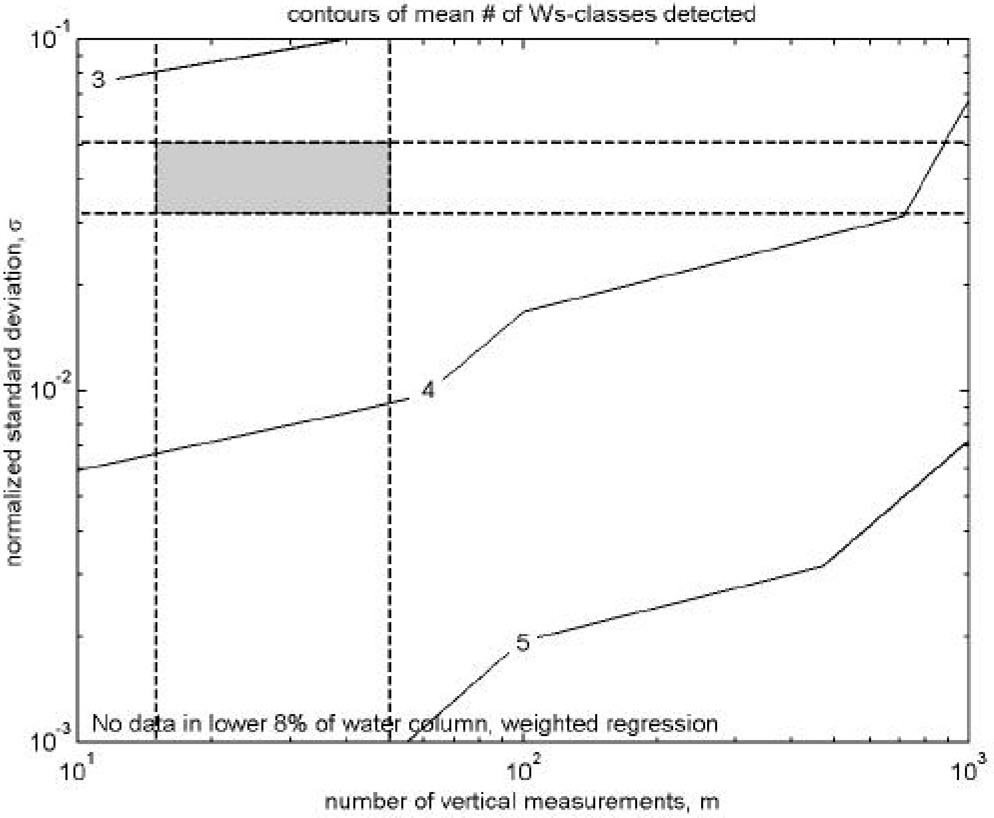

Figure 15, right panel

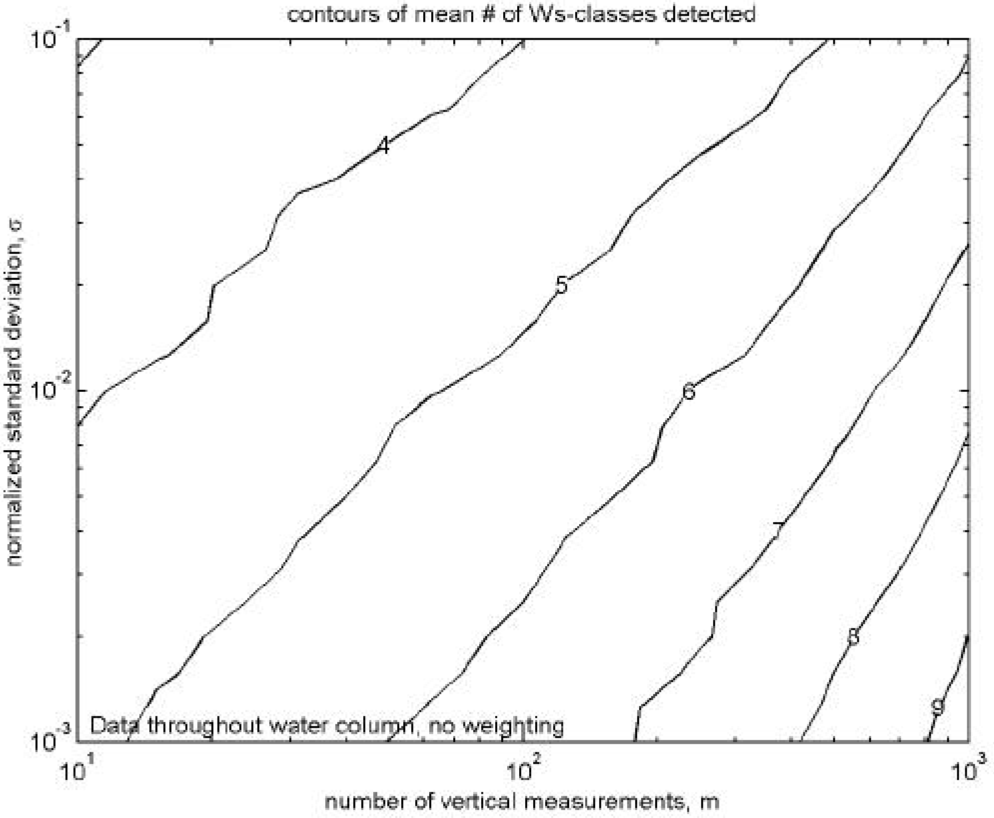

Figure 15: Contours of the optimal number of *Ws*-classes in Step 2, the model-dependent decomposition. In the left panel, we show the optimal number for the Fraser calibration. The range in number of evenly-spaced vertical grid points (*m*) and the optical and acoustic standard deviation (s) are marked with dashed lines and a shaded area for reference. In the right panel, it is assumed that no regression weighting is necessary and data are present throughout the water column. Details are given in **Section 6.1**.